JGR Earth Surface

RESEARCH ARTICLE
10.1029/2021JF006239

Groundwater Affects the Geomorphic and Hydrologic Properties of Coevolved Landscapes

David G. Litwin[1], Gregory E. Tucker[2,3], Katherine R. Barnhart[2,3,4], and Ciaran J. Harman[1,5]

[1]Department of Environmental Health and Engineering, Johns Hopkins University, Baltimore, MD, USA, [2]Cooperative Institute for Research in Environmental Sciences (CIRES), University of Colorado, Boulder, CO, USA, [3]Department of Geological Sciences, University of Colorado, Boulder, CO, USA, [4]Now at U.S. Geological Survey, Geologic Hazards Science Center, Golden, CO, USA, [5]Department of Earth and Planetary Science, Johns Hopkins University, Baltimore, MD, USA

Key Points:

- Presents a coupled model of shallow groundwater and landscape evolution to examine coevolution of runoff generation and landscape morphology
- Analysis of the model suggests that hillslope length scales nonlinearly with subsurface drainage capacity relative to the recharge rate
- Emergent morphology can be characterized by three metrics (steepness, curvature, topographic index) and is controlled by four dimensionless numbers

Supporting Information:

Supporting Information may be found in the online version of this article.

Correspondence to:

C. J. Harman,
charman1@jhu.edu

Citation:

Litwin, D. G., Tucker, G. E., Barnhart, K. R., & Harman, C. J. (2022). Groundwater affects the geomorphic and hydrologic properties of coevolved landscapes. *Journal of Geophysical Research: Earth Surface*, *127*, e2021JF006239. https://doi.org/10.1029/2021JF006239

Received 29 APR 2021
Accepted 5 NOV 2021

Abstract The hydrologic dynamics and geomorphic evolution of watersheds are intimately coupled—runoff generation and water storage are controlled by topography and properties of the surface and subsurface, while also affecting the evolution of those properties over geologic time. However, the large disparity between their timescales has made it difficult to examine interdependent controls on emergent hydrogeomorphic properties, such as hillslope length, drainage density, and extent of surface saturation. In this study, we develop a new model coupling hydrology and landscape evolution to explore how runoff generation affects long-term catchment evolution, and analyze numerical results using a nondimensional scaling framework. We focus on hydrologic processes dominating in humid climates where storm runoff primarily arises from shallow subsurface flow and from precipitation on saturated areas. The model solves hydraulic groundwater equations to predict the water-table elevation given prescribed, constant groundwater recharge. Water in excess of the subsurface capacity for transport becomes overland flow, which generates shear stress on the surface and may detach and transport sediment. This affects the landscape form that in turn affects runoff generation. We show that (a) four dimensionless parameters describe the possible steady state landscapes that coevolve under steady recharge; (b) hillslope length increases with increasing transmissivity relative to the recharge rate; (c) three topographic metrics—steepness index, Laplacian curvature, and topographic index—together provide a basis for interpreting landscapes that have coevolved with runoff generated via shallow subsurface flow. Finally we discuss the possibilities and limitations for quantitative comparisons between the model results and real landscapes.

Plain Language Summary Watersheds store and release water in response to precipitation in complex ways that are strongly affected by topography and subsurface properties. However, over long timescales (thousands to millions of years), the flow of water plays a critical role in shaping these attributes through processes like erosion and subsurface weathering. Consequently, we expect many places have key links between their topographic form and hydrological properties. We present a new model to explore these effects, focusing on the feedbacks between surface erosion and runoff generation from seepage of shallow groundwater and precipitation on saturated areas. Runoff can detach sediment, changing the topography. Topographic slope is in turn a driving force of groundwater flow. By grouping the model parameters together, we develop a set of "knobs" that we can "turn" to explore the model output. We find that when the subsurface has greater capacity to transmit water (relative to the precipitation supplied), the spacing between stream channels is greater. The results illuminate key topographic properties of landscapes that evolve with shallow groundwater, though much work remains before we can adequately compare results from this type of model with data.

1. Introduction

1.1. Motivation

Landscape morphology and subsurface structure are strong predictors of runoff generation style and spatial distribution (Dunne, 1978). In humid climates, the infiltration capacity of undisturbed soil is high and overland flow due to exceedance of soil infiltration capacity is rare. When relief is relatively low and soils are relatively thin, runoff is most commonly generated by the expansion of variable source areas, which may generate overland flow where precipitation falls directly on saturated areas (Dunne & Black, 1970). In steeper landscapes with deep soils, water may be transmitted laterally through the subsurface at permeability contrasts, becoming surface

runoff only when it reaches stream channels (Hewlett & Hibbert, 1967). Saturated areas (including wetted stream channels) emerge as the supply of water from upslope areas exceeds the conveyance capacity of water through the subsurface. This competition between upslope supply and downslope transport capacity links properties of the subsurface, such as transmissivity, to the runoff response of watersheds as a whole (O'Loughlin, 1981). Furthermore, overland flow generates shear stress on the land surface that may detach and transport sediment. This drives the evolution of topographic convergence/divergence and convexity/concavity, which are important controls on runoff generation themselves (Lapides et al., 2020; Prancevic & Kirchner, 2019; Troch et al., 2003). Research also suggests that incision and hillslope sediment transport play a role in setting the rate and extent of subsurface weathering by setting the rate at which fresh bedrock is supplied to the near surface (Gabet & Mudd, 2009; West et al., 2005). Weathering is in turn crucial for setting subsurface properties including porosity and hydraulic conductivity that affect groundwater flow and storage capacity.

These feedbacks further suggest that there should be intimate links between runoff generation behavior and landscape morphology (Jefferson et al., 2010; Manga, 1996; Yoshida & Troch, 2016). The long timescales of geomorphic evolution limit our ability to study these relationships directly. An alternative approach is to examine signatures of these processes in observable landscape morphology. Topographic metrics including drainage density, channel steepness, curvature, and topographic (wetness) index have been essential in understanding hydrologic and geomorphic processes in the past. However, it is unclear how these metrics might encode aspects of the coevolution of landscape morphology and hydrological processes. If morphology affects and is affected by runoff generation, how might long-term evolution affect emergent topographic properties and the extent of surface saturation in a landscape? Here we will draw insights from a coupled hydrogeomorphic model in which we can examine the emergent features of landscapes evolved with known subsurface properties and runoff generation mechanisms.

1.2. Previous Representations of Runoff Generation in Landscape Evolution Models

Over geologic time, upland landscapes are shaped by the competition between incision by overland flow, gravitationally driven fluxes of sediment due to processes including biogenic disturbance and frost heaving, and baselevel change (Howard, 1994). While it is not possible to observe the evolution of landscapes at human timescales, numerical landscape evolution models (LEMs) have allowed researchers to make substantial progress in understanding how landscapes respond to dynamic forcings of tectonics, lithology, and climate (e.g., reviews by Bishop, 2007; Chen et al., 2014; Martin & Church, 2004; Pazzaglia, 2003; Pelletier, 2013; Temme et al., 2013; Valters, 2016). However, the treatment of hydrology in models that consider evolution over geologic time remains rudimentary.

Early LEMs treated runoff as the product of upslope area and an effective precipitation rate (Ahnert, 1976; Armstrong, 1976; Willgoose et al., 1991a), representing the time-averaged runoff from infiltration excess overland flow. In these models, all areas of the landscape generated surface runoff simultaneously, though all areas might not experience erosion due to the presence of thresholds for sediment detachment (Horton, 1945). The practice of using such runoff formulations in LEMs is still common today when hydrologic response is not central to the study, as models with minimal hydrologic dynamics can still effectively capture certain essential aspects of landscape form (e.g., Barnhart, Tucker, Doty, Glade, et al., 2020; Forte et al., 2016; Theodoratos et al., 2018). One of the first attempts to capture subsurface hydrology in a LEM was the model developed by Ijjász-Vásquez et al. (1992), in which precipitation was partitioned between surface and subsurface flow using a steady-state topographic index criterion (Beven & Kirkby, 1979). The authors found that this partitioning significantly changed catchment hypsometry in comparison to the infiltration excess formulation. Tucker and Bras (1998) compared several different landscape evolution and runoff generation formulations, including one that treated subsurface transport capacity similarly to Ijjász-Vásquez et al. (1992). They found that the evolved landscapes have sharp hillslope-valley transitions at a critical value of topographic index. These transitions were smoothed by treating precipitation as a random process with an exponential distribution, rather than having a single value. However, the topographic index type models neglect the role of nonlinearities in groundwater flow, and antecedent conditions that determine catchment runoff response to precipitation. We refer to flow nonlinearity as the degree to which groundwater flow is driven by diffusion due to gradients in aquifer thickness rather than kinematic wave motion in which flow is driven by the slope of permeability contrasts, which can have significant effects on runoff generation (Harman & Sivapalan, 2009). The steady-state assumption of the topographic index model assumes

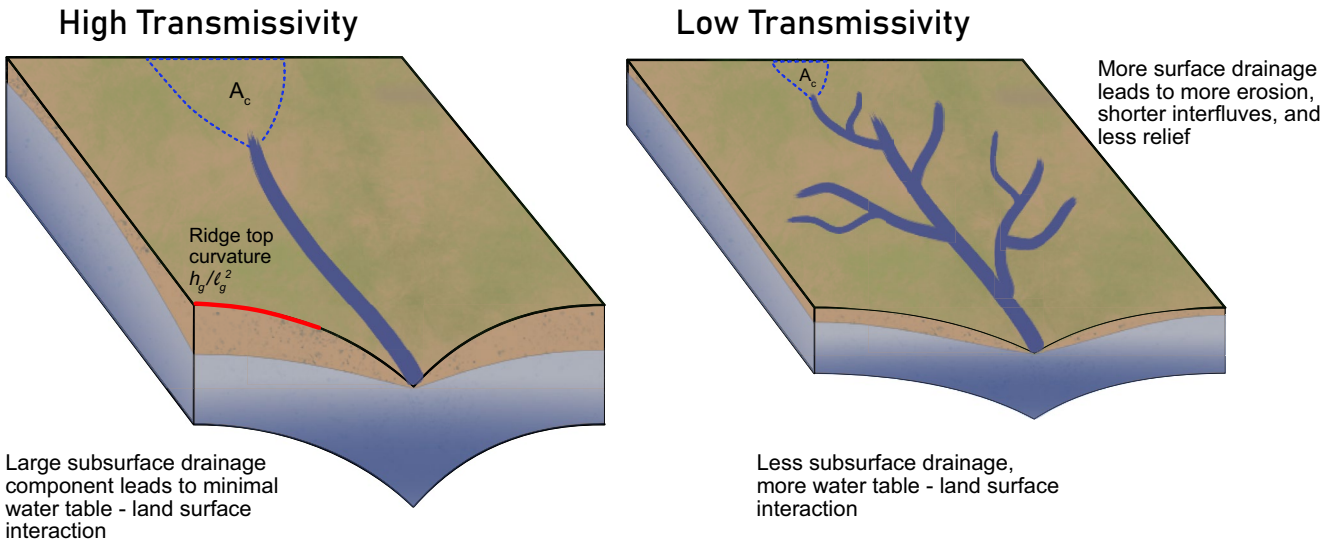

Figure 1. Illustration of two landscapes showing hypothesized differences in morphology with subsurface transmissivity given same geologic and climatic setting. The lower transmissivity landscape (right) transports less water through the subsurface, and therefore has smaller subsurface contributing areas before flow emerges at the surface. The greater extent of surface flow results in greater dissection, as reflected in the development of a denser drainage network with lower-relief interfluves.

that a storm event is effectively independent of prior events, and arrives with the full subsurface capacity available to drain flow. Many hydrological studies have shown that antecedent conditions are important controls on runoff magnitudes, where wetter systems are primed for larger runoff response due to lack of available subsurface storage or transport capacity (Brocca et al., 2009; Tramblay et al., 2010).

Several studies have coupled landscape evolution with hydrological processes in greater detail. Huang and Niemann (2006) and Huang and Niemann (2008) developed a coupled groundwater model and LEM, and demonstrated the importance of dynamic runoff generation mechanisms for the topographic evolution of different areas of modeled basins. Huang and Niemann (2006) focused on the evolution of a single well-studied catchment, and found that as they simulated its evolution from present, runoff was increasingly generated by subsurface lateral flow rather than saturation excess overland flow. Huang and Niemann (2008) explored the long-term geomorphic evolution of synthetic catchments with groundwater flow, and concluded that the hypsometry of steady-state landscapes was not generally distinguishable between surface water-dominated and groundwater-dominated landscapes. However, sensitivity of modeled topography to parameters was conducted by imposing changes directly onto the slope area relationship, rather than examining results of the coupled model, making it difficult to evaluate the precise role of groundwater flow in long-term evolution. Zhang et al. (2016) presented a highly detailed, coupled hydrological model and LEM, though to our knowledge it has not been used beyond the initial proof of concept. With solutions to Richards equation for subsurface flow and St. Venant's equation for surface flow and employment of several dozen parameters, this model is computationally expensive and may be more complex than needed to explore process feedbacks between shallow subsurface hydrology and landscape evolution. A systematic approach is needed to understand these feedbacks. It must be simple enough for interpretation of process controls while still having the core elements of landscape evolution and dynamic runoff generation from the shallow subsurface.

1.3. Scaling and Dimensionless Landscape Morphology

The generation of surface runoff can be seen as the failure of the subsurface to drain precipitation inputs. The transmissivity of the subsurface (i.e., the hydraulic conductivity integrated over the permeable thickness) is a major control on that drainage capacity, and so intuitively, the transmissivity should vary inversely with the degree of surface drainage dissection, as illustrated in Figure 1. Reducing the transmissivity increases partitioning of water into surface flow, which results fluvial incision closer to drainage divides (Carlston, 1963). This suggests that transmissivity controls some length scale embedded in the landscape morphology. In this paper, we aim to understand the nature of this control under idealized model assumptions.

Scaling and dimensional analysis offer a powerful systematic approach for investigating models described by partial differential equations. In general, this approach allows the governing equations to be expressed in a dimensionless form, fundamental length and time scales to be identified, and dimensionless parameters controlling the scale-independent qualitative characteristics of solutions to be obtained (Barenblatt, 1996). Studies of LEMs have used such analyses to great effect, uncovering the inherent scaling properties of simple LEMs (Bonetti et al., 2020; Perron et al., 2008; Theodoratos et al., 2018; Willgoose et al., 1991b). For example Theodoratos et al. (2018) developed a dimensionless form of a simple LEM with no dimensionless parameters in the main governing equation, suggesting that all solutions were simply rescaled versions of each other (up to differences in boundary and initial conditions). Bonetti et al. (2020) conducted a similar approach, but found that one dimensionless parameter remained in the LEM. (Note: we resolve this apparent contradiction in Section 4).

However, these prior studies have not considered the role of subsurface properties or hydrology. We aim to use scaling and dimensional analysis to reveal how transmissivity controls these fundamental scales and morphologic characteristics. It will also reveal how the transmissivity interacts with scales controlled by other parameters, such as those that determine the curvature of ridge tops that do not experience runoff.

1.4. Approach

In this study, we develop and use a new groundwater-landscape evolution model to explore how subsurface-mediated runoff generation affects long-term catchment evolution. The model solves hydraulic groundwater equations to predict the water-table elevation given prescribed recharge. Water in excess of the subsurface flow capacity becomes overland flow, which may detach and transport sediment, altering topographic properties that in turn affect runoff generation. Our model can support recharge rates which vary in space and time, but here we constrain the scope and consider only steady, uniform recharge. We conduct a scaling analysis that provides new insight into the dynamics behind the widely used "stream power plus diffusion" model. This analysis makes predictions which we test with a series of model simulations. Additionally, the nondimensionalization generalizes our results and reconciles conflicting dimensional analyses provided by Theodoratos et al. (2018) and Bonetti et al. (2020). We can reduce the seven dimensioned parameters of the model to four dimensionless parameters, one of which is always negligible. We present numerical results confirming the efficacy of our nondimensionalization and exploring the newly defined nondimensional parameter space to determine how hydrologic and geomorphic parameters affect emergent hydrogeomorphic properties at geomorphic steady state. The results show that subsurface flow capacity relative to recharge rate exerts a fundamental control on hillslope length. Additionally, an emergent relationship between three topographic metrics derived from the governing equations captures the coevolution of runoff generation and topography according to the processes considered in this study.

2. Governing Equations

To investigate the effects of subsurface hydrology on landscape evolution, we couple a hydrological model to a standard model of landscape evolution. First, we derive a governing equation for topographic evolution that includes the role of space- and time-variable runoff in fluvial incision. Second, we examine the hydrological model that will generate runoff. Variable dimensions are provided in Notation.

2.1. Landscape Evolution

Topographic elevation $z(x, y, t)$ is assumed to evolve due to fluvial incision $E_f(x, y, t)$, hillslope diffusion $E_h(x, y, t)$, and constant baselevel change U.

$$\frac{\partial z}{\partial t} = -E_f - E_h + U \tag{1}$$

The term E_f accounts for incision into the landscape by erosion due to overland flow. The term E_h accounts for gravitational soil-transport processes that tend to smooth out landscape features. The term U accounts for the constant rate of either tectonic uplift or baselevel fall, in this case increasing topographic elevation relative to a fixed elevation boundary.

In one commonly used form of this equation, fluvial incision is described by the streampower law, originally derived from empirical data (Howard & Kerby, 1983):

$$E_f = KA^m|\nabla z|^n \tag{2}$$

Here $A(x, y, t)$ is the upslope drainage area. In the standard streampower formulation, the exponents are $m = 1/2$ and $n = 1$. This is supported by observations of stream profile concavity that suggest $m/n \approx 0.5$, and a derivation in which incision is proportional to streampower per unit surface area, while channel width increases with the square root of discharge (Barnhart, Tucker, Doty, Shobe, et al., 2020; Whipple & Tucker, 1999). This gives the streampower incision law:

$$E_f = K\sqrt{A}|\nabla z| \tag{3}$$

This equation obscures the role of hydrological processes in the fluvial incision that drives landscape evolution. The relationship in Equation 3 can also be derived from first principles in a way that provides a natural coupling to hydrological processes. This is accomplished by assuming the incision rate E_f is related to the excess shear stress τ from overland flow by some power-law relationship. Frequently, this is written in the form:

$$E_f = k_e(\tau - \tau_c)^\beta \tag{4}$$

This excess shear stress formulation assumes that sediment is not redeposited within the domain (meaning that the system is assumed to be "detachment-limited"), which is widely used for upland watersheds (Howard, 1994). Here τ_c is the threshold shear stress below which sediment will not be detached. Our model will also manifest a threshold in τ due to the explicit partitioning of water flow between subsurface and surface. The effects of these thresholds are not the same; while both fluvial incision and runoff generation have a dependence on slope, a steeper slope yields greater fluvial incision but less surface water flow. To focus on the spatial variation in erosion associated with hydrological processes, we will examine only the case in which there is no threshold shear stress for sediment detachment, such that $\tau_c = 0$. The shear stress generated by steady, uniform flow in a rectangular channel is:

$$\tau = \rho_w g d_f |\nabla z|, \tag{5}$$

where ρ_w is the density of water, g is the acceleration due to gravity, and d_f is the flow depth. A constitutive relation for flow resistance such as the Manning or Chezy equation can provide the flow depth d_f at a particular discharge Q. We use the Chezy equation for simplicity, which gives:

$$d_f = \left(\frac{Q}{Cw\sqrt{|\nabla z|}}\right)^{2/3} \tag{6}$$

Here we assume that the channel width w is proportional to the square root of upslope area (e.g., Snyder et al., 2003; Wohl & David, 2008):

$$w \sim \sqrt{A} \tag{7}$$

As we will show in the subsequent scaling analysis, it will be useful to express w in terms of area per contour width $a(x, y, t)$. However, the hydraulic scaling relationships for channel width are defined on the basis of catchment area A at a given cross-section (Leopold & Maddock, 1953). To make the conversion between A and a, we represent A as the product of a and a characteristic contour width v_0, which is a chosen constant value. We will examine the physical significance of this parameter in later sections. To obtain values for w from Equation 7 we additionally require the dimensionless parameter k_w:

$$w = k_w\sqrt{v_0 a} \tag{8}$$

In this equation there is only one degree of freedom, so we are free to choose a value of v_0 for which there will always be a corresponding value of k_w to satisfy a given relationship between a and w. Ultimately, k_w will become a component of the streampower coefficient K, while here v_0 remains separate, and has additional significance in the context of hydrological processes.

Next, we write the discharge $Q(x, y, t)$ as the product of an instantaneous runoff ratio $Q^*(x, y, t)$, upslope area A, and the average recharge rate p, $Q = pAQ^*$, and substitute into Equations 5 and 6 to find the flow depth and shear stress.

$$d_f = \left(\frac{Q^* p \sqrt{v_0 a}}{C k_w \sqrt{|\nabla z|}} \right)^{2/3} \tag{9}$$

$$\tau = \rho_w g \left(\frac{Q^* p \sqrt{v_0 a}}{C k_w \sqrt{|\nabla z|}} \right)^{2/3} |\nabla z| \tag{10}$$

To recover the stream power formulation of the fluvial incision term, we set $\beta = 3/2$ (Tucker, 2004) in Equation 4, representative of hydraulic detachment by plucking (Tsujimoto, 1999; Whipple et al., 2000). With these substitutions, the incision rate E_f can be written as:

$$E_f = K \sqrt{v_0} Q^* \sqrt{a} |\nabla z| \tag{11}$$

where $K = \frac{(\rho_w g)^{3/2} k_e p}{C k_w}$. This form is equivalent to Equation 3, with time and space varying runoff accounted for in Q^*. Additionally because Q^* is dimensionless, K in Equation 11 has units of $[1/T]$, the same as in Equation 3.

The upslope area A is usually defined by explaining the algorithms used to calculate it in numerical schemes, which find flow directions on a discrete grid and sum the grid cell areas downslope along these flow directions. However, this approach gives the area an implicit dependence on grid cell spacing. Area per contour width a on the other hand has a precise mathematical definition that can be derived from conservation of mass (Bonetti et al., 2018, 2020). Consider the steady-state depth of water h_f across a surface where all locations contribute runoff at the same rate r. Conservation of mass for this system indicates that $\nabla \cdot (h_f u) = r$, where u is the (vector) flow velocity. Now suppose that the flow velocity at every point also has magnitude r and points in the direction of steepest descent $-\nabla z/|\nabla z|$. To satisfy continuity with this velocity, the flow depth must increase downslope. In fact, the flow depth is equal to the upslope area per contour width, $h_f = a$ (Bonetti et al., 2018). This derivation shows that, by definition:

$$-\nabla \cdot \left(a \frac{\nabla z}{|\nabla z|} \right) = 1. \tag{12}$$

We are not implying that the assumptions we have made here are necessarily characteristics of all real flow; rather these assumptions can be employed, without violating conservation of mass, to develop a condition that area per contour width must satisfy. This expression will become important in our scaling analysis in later sections, as the scaling properties of the governing equations should be independent of the numerical implementation where a grid cell width must be chosen.

Here we use a linear diffusion model of hillslope processes for E_h, which emerges by assuming that the non-fluvial sediment transport rate q_h is proportional to the local slope gradient $-\nabla z$, much as diffusion of a solute is proportional to the concentration gradient (Dietrich et al., 2003). Then by assuming $E_h \sim \nabla \cdot q_h$ from continuity, we find:

$$E_h = -D \nabla^2 z, \tag{13}$$

where D is the linear diffusion constant. While nonlinear formulations of diffusion have proven useful in explaining topography (Roering, 2008; Roering et al., 1999), here we use linear diffusion to limit model complexity. We assume that baselevel change has a constant rate U in time and space by adopting a frame of reference anchored to baselevel at the boundary of the domain. This can equivalently represent tectonic uplift or baselevel fall. This term becomes a "source" in the differential equation; without it, the topography would simply erode to a flat plane. While baselevel change is likely not steady in time in real landscapes, this assumption allows us to examine the emergent properties of steady-state solutions to the governing equations. Combining all terms together, we arrive at our governing equations for topographic evolution:

$$\frac{\partial z}{\partial t} = -K \sqrt{v_0} Q^* \sqrt{a} |\nabla z| + D \nabla^2 z + U \tag{14}$$

$$-\nabla \cdot \left(a \frac{\nabla z}{|\nabla z|} \right) = 1 \tag{15}$$

This is different from the standard streampower formulation of landscape evolution in that it includes a dimensionless runoff coefficient Q^* to account for the spatial and temporal variation in runoff across the landscape. While there is considerable uncertainty in the form of the fluvial incision term, the similarity between the form we have selected and the standard "stream power plus diffusion" formulation allows us to make use of the same nondimensionalization techniques used for the standard LEM, and has properties that will aid in implementation and analysis of results while remaining plausible within the context of the existing literature.

2.2. Hydrology

Thus far, we have made no assumptions regarding the hydrology, instead introducing a general dimensionless runoff rate $Q^* = Q/(pA)$. Any approach to representing hydrology could use the above equations by calculating appropriate values for Q^*. In our application surface water runoff is assumed to be generated by exfiltrating subsurface lateral flow (Hewlett & Hibbert, 1967) and by precipitation on saturated areas (Dunne & Black, 1970). We solve for this runoff using a quasi-3D shallow unconfined aquifer model using the Dupuit-Forcheimer approximations (e.g., Childs, 1971). The approximations are valid in locations where the vertical component of groundwater flow is small—generally where saturated thickness is small relative to hillslope or seepage face length (Bresciani et al., 2014). While this may not be the case everywhere in our model parameter space, we are using the approximations because we cannot feasibly complete the landscape evolution simulations with the full 3D representation due to computational cost. A model of this type represents a worthwhile trade-off between accuracy and efficiency at this stage in the development of coupled groundwater-LEMs. We solve the model for lateral groundwater flow $q(x, y, t)$, and local runoff production $q_s(x, y, t)$. This model makes use of a method of regularization introduced by Marçais et al. (2017) in solving for q_s that greatly improves model stability at seepage faces. Surface water discharge is calculated by instantaneously routing q_s and integrating the accumulated local runoff over the area upslope of a given location. The governing equations for the hydrological model are:

$$\frac{\partial h}{\partial t} = \frac{1}{n_e}(p - \nabla \cdot q - q_s) \tag{16}$$

$$q = -h\cos\theta k_s(\nabla z_b + \nabla h)\cos\theta \tag{17}$$

$$q_s = \mathcal{G}\left(\frac{h}{b}\right)\mathcal{R}(i - \nabla \cdot q) \tag{18}$$

$$Q = \int_A q_s \, dA \tag{19}$$

where $h(x, y, t)$ is the aquifer thickness, n_e is the effective or drainable porosity, $\theta(x, y, t)$ is the local slope of the (presumed impermeable) aquifer base, z_b is the elevation of the aquifer base, k_s is the saturated hydraulic conductivity, and b is the permeable thickness. The regularization function $\mathcal{G}(\cdot)$ has a value of zero when the argument is less than one, and approaches 1 as the argument approaches 1. The ramp function $\mathcal{R}(\cdot)$ is zero when the argument is less than zero and takes on the argument value when it is greater than zero.

Though this model can accommodate time-variable recharge, here we consider only constant recharge at rate p. Careful examination of this model reveals that saturated areas receive "recharge" at the same rate as areas with deeper water-tables. In reality, saturated areas receive direct precipitation, while areas with deeper water tables receive a smaller fraction as a result of losses to unsaturated zone storage and evapotranspiration from the root zone. When saturated area is a small proportion of the total area and the water table is not too deep, this effect may be negligible. We will leave further investigation on the role of unsaturated zone dynamics to a future contribution, as this would add considerable complexity to the model.

In the cases modeled here, the permeable thickness b is treated as constant in space and time. As our model does not distinguish between mobile soil or regolith and in-place weathered or fractured rock, we will use permeable thickness as a general term for the entire permeable zone in which the shallow aquifer must be contained. Considerable uncertainty exists in the rates and mechanisms that convert fresh bedrock to permeable fractured

rock and/or regolith. Many past models have used an exponential function for the production of regolith (e.g., Ahnert, 1976; Armstrong, 1976; Rosenbloom & Anderson, 1994; Tucker & Slingerland, 1997), where the production rate is a function of regolith thickness. Permeable thickness may be considered to follow a similar law, in that it tends to be thicker where the materials are more susceptible to weathering processes, where a wetter climate allows for more active subsurface weathering, and/or where erosion rates are lower. At geomorphic steady state, both the rates of change of topographic elevation and unweathered bedrock elevation go to zero. For the latter to be the case, the production rate of weathered material must be equal to the uplift rate. When the uplift rate and regolith production coefficients are spatially uniform, permeable thickness must also be uniform to satisfy this equilibrium. This suggests that it is reasonable to treat permeable thickness as steady and uniform across the model domain given that we are only concerned with steady-state landforms in this paper.

3. Numerical Implementation

3.1. Timescale Considerations

One of the primary challenges in coupling a hydrological model with a landscape evolution model is the vast difference in process timescales. While the relevant timescale for storm runoff response may be on the order of hours or even minutes, landscape evolution processes can have characteristic timescales on the order of tens to thousands of years. It would be too computationally expensive to run models over geologic time using appropriately small timesteps for stability and accuracy of the hydrological model. Zhang et al. (2016) identified two approaches to address this problem: online updating and offline updating. In the offline case, the hydrological model is run for many timesteps without updating topography, and then appropriately averaged discharge values are used to update topography over some larger geomorphic timestep. In contrast, online updating involves having a direct scaling between the hydrological timestep (e.g., one storm event) and the geomorphic timestep. Zhang et al. (2016) used an online approach, citing possible non-uniqueness of solutions in the offline approach depending on the time between geomorphic updates. Given that we consider only steady recharge in this paper, there should not be a significant difference between online and offline approaches, as the hydrological state varies gradually, only in response to changing topography. Nonetheless, our approach can be considered online updating, as we scale the geomorphic timestep as k_{sf} times the hydrological timestep: $\Delta t_g = k_{\mathrm{sf}} \Delta t_h$. We call k_{sf} the timestep scaling factor.

3.2. Model Implementation

The groundwater and landscape evolution models described above were implemented in the DupuitLEM Python package, which makes extensive use of existing tools from the Python-based Earth surface modeling toolkit Landlab (Barnhart, Hutton, et al., 2020; Hobley et al., 2017). Landlab includes tools for creating grids, setting boundary conditions, handling input and output, along with a diverse range of process components that modify fields on Landlab grids according to physical laws. The groundwater model described above is implemented as a component in Landlab called GroundwaterDupuitPercolator (Litwin et al., 2020).

DupuitLEM can operate on raster, hexagonal, and irregular grids with zero-flux and fixed value boundary conditions. The model base class takes components that update the hydrological state via hydrological fluxes and changes in boundary conditions, update topography via fluvial incision, hillslope diffusion, and baselevel change, and update permeable thickness via regolith production. Here we use the DupuitLEM subclass StreampowerModel, designed for use with the Landlab fluvial incision component FastscapeEroder, which solves a modified version of the Fastscape algorithm (Braun & Willett, 2013).

The hydrological state is updated with a DupuitLEM HydrologicalModel. All hydrological models solve for aquifer state and fluxes using the GroundwaterDupuitPercolator component. Surface water discharge is routed instantaneously using a D8 algorithm when the grid is a raster, or a steepest descent algorithm otherwise. In the case of steady recharge, we use the HydrologicalModel subclass HydrologySteadyStreamPower, which updates the surface water discharge by advancing the GroundwaterDupuitPercolator, finding surface flow directions including routing through topographic depressions, and accumulating q_s along flow directions to determine Q. With known area A and recharge rate p, we can calculate the runoff ratio $Q^* = Q/(pA)$ that appears in our streampower model, linking the hydrology to geomorphic evolution. We use a raster grid with dimensions 125 × 125, with three zero-flux boundaries (right, left, top) and one fixed value boundary along the bottom of the model domain.

The geomorphic timestep in all simulations is 45 years, while the hydrologic timestep varies as a multiple of the von Neumann stability criteria, taking values from approximately four hours to three days. The adaptive timestep solver of the GroundwaterDupuitPercolator will further subdivide the timestep to meet stability criteria, while surface flow is only routed at this interval.

4. Scaling and Similarity

A similarity analysis of the governing equations illuminates their fundamental controls and will guide the investigation conducted in the rest of this paper. Here we use an approach based on the concept of symmetry groups (Barenblatt, 1996). A symmetry group is a set of scaling transformations of variables and parameters by a constant factor that leave the governing equations unchanged due to cancellation of that factor. In essence, we seek to identify the complete set of symmetry groups and apply transformations such that we consolidate or eliminate parameters that appear in the equations. Using this approach we arrive at a general form of the governing equations where dimensional parameters appear in dimensionless groups. We use these emergent dimensionless parameters in our numerical experiments, greatly reducing the size of the parameter space to explore and exposing relationships between model parameters.

4.1. *NoHyd* Model

We will begin this process by considering the simplest version of the model without space- or time-variable runoff, such that $Q^*(x, y) = 1$ everywhere. We will call this the *NoHyd* model. The symmetry group analysis is most easily conducted when the model parameters have been rewritten as the product of characteristic scales, isolating each dimension (time, length, etc.). Theodoratos et al. (2018) determined that there are unique characteristic scales for the vertical coordinate, the horizontal coordinate, and time h_g, ℓ_g, t_g that emerge from the "streampower plus diffusion" landscape evolution equations. Based on their analysis, we can rewrite Equations 14 and 15 in terms of these scales without changing the units of the state variables.

$$t_g \frac{\partial z}{\partial t} = -\sqrt{\ell_g} Q^* \sqrt{a} |\nabla z| + \ell_g^2 \nabla^2 z + h_g \tag{20}$$

$$-\nabla \cdot \left(a \frac{\nabla z}{|\nabla z|} \right) = 1 \tag{21}$$

Because we have replaced three parameters, K, D, and U, in Equation 14 three characteristic scales, h_g, ℓ_g, and t_g, we can derive a system of equations for their relationships: $U = h_g/t_g$, $D = \ell_g^2/t_g$, $K\sqrt{v_0} = \sqrt{\ell_g}/t_g$. We can solve this system for the characteristic scales:

$$h_g = \left(\frac{DU^3}{v_0^2 K^4} \right)^{1/3} \tag{22}$$

$$\ell_g = \left(\frac{D^2}{v_0 K^2} \right)^{1/3} \tag{23}$$

$$t_g = \left(\frac{D}{v_0^2 K^4} \right)^{1/3}. \tag{24}$$

These definitions are slightly different from those of Theodoratos et al. (2018), as we use the area per contour width a as a state variable rather than using drainage area A. Next we will identify the symmetry groups. We find that there are three groups, each of which allows us to scale two or more dimensioned variables by an arbitrary factor $c > 0$ and leave Equations 20 and 21 unchanged.

$$\{t \to ct, \;\; t_g \to ct_g\} \tag{25}$$

$$\{z \to cz, \;\; h_g \to ch_g\} \tag{26}$$

$$\{x \to cx,\ \ y \to cy,\ \ a \to ca,\ \ l_g \to cl_g\} \tag{27}$$

The notation above can be read as, for example, "replace each occurrence of t by ct," and similarly for each set of symbols separated by a right-pointing arrow. For example, consider applying the first symmetry group by replacing every occurrence of t with ct. We find that when doing this, we must also replace every occurrence of t_g with ct_g in order for all c's to cancel. The same principle applies to the other groups as well. Note that the final group also requires that we transform the gradient operator: $\nabla^2 z \to c^{-2}\nabla^2 z$ and $|\nabla z| \to c^{-1}|\nabla z|$, as a consequence of the transformations of x and y.

Because these symmetry groups apply for any c > 0, we can simplify the governing equations by choosing values of c such that the characteristic scales h_g, ℓ_g, and t_g do not appear in the equations. For example, we can apply the first symmetry group, taking $c = 1/t_g$, resulting in the transformations $\{t \to t/t_g,\ t_g \to 1\}$. In doing so, we have effectively rescaled t into units of t_g. We will denote this dimensionless time as $t' = t/t_g$. Likewise, we can take a similar approach with application of the other symmetry groups:

$$\begin{gathered}\{t \to t/t_g,\ \ t_g \to 1\} \\ \{z \to z/h_g,\ \ h_g \to 1\} \\ \{x \to x/\ell_g,\ \ y \to y/\ell_g,\ \ a \to a/\ell_g,\ \ l_g \to 1\}\end{gathered} \tag{28}$$

Applying all three transformations and defining the dimensionless state variables

$$\begin{aligned}t' &= t/t_g \\ z' &= z/h_g \\ x' &= x/\ell_g \\ y' &= y/\ell_g \\ \nabla' &= \nabla\ell_g \\ a' &= a/\ell_g\end{aligned} \tag{29}$$

we obtain the dimensionless governing equations for the landscape evolution model:

$$\frac{\partial z'}{\partial t'} = -\sqrt{a'}|\nabla' z'| + \nabla'^2 z' + 1 \tag{30}$$

$$-\nabla' \cdot \left(a' \frac{\nabla' z'}{|\nabla' z'|}\right) = 1 \tag{31}$$

No parameters appear in these rescaled equations. Intuitively, this demonstrates that all possible solutions of the *NoHyd* model can be obtained by appropriately rescaling any other solution given identical boundary and initial conditions. We would not obtain a fully parameterless model if we had chosen to write the equations in terms of area A rather than area per unit contour width a. In that case, a single parameter v_0/ℓ_g would appear in Equation 31. Not accounting for this parameter effectively leaves a grid cell size dependence in the nondimensionalization, which is something we seek to avoid.

4.2. *DupuitLEM* Model

Next we relax our constraint of uniform dimensionless runoff ($Q^* = 1$) and incorporate the hydrological equations into the scaling analysis. This model is called *DupuitLEM*. The scaling analysis of this model extends the analysis of the *NoHyd* model, and can be found in Appendix A. To complete the analysis, we introduce two new characteristic scales: a characteristic aquifer drainage time t_d and a characteristic aquifer thickness h_a (which are also reproduced in Equations A3 and A4 respectively):

$$h_a = \frac{p\ell_g}{k_s h_g/\ell_g} \tag{32}$$

$$t_d = \frac{\ell_g n_e}{k_s h_g / \ell_g}. \tag{33}$$

The dimensionless governing equations for the *DupuitLEM* model are:

$$\frac{\partial z'}{\partial t'} = -Q^* \sqrt{a'} |\nabla' z'| + \nabla'^2 z' + 1 \tag{34}$$

$$-\nabla' \cdot \left(a' \frac{\nabla' z'}{|\nabla' z'|} \right) = 1 \tag{35}$$

$$\delta \frac{\partial h'}{\partial t} = 1 - \nabla' \cdot q' - q'_s \tag{36}$$

$$q' = -h' \cos^2(\arctan|\alpha \nabla' z'|)(\nabla' h' / \mathrm{Hi} + \nabla' z') \tag{37}$$

$$= -h' \frac{\nabla' h' / \mathrm{Hi} + \nabla' z'}{1 + \alpha^2 |\nabla' z'|^2} \tag{38}$$

$$q'_s = \mathcal{G}(h'/\gamma)\mathcal{R}(1 - \nabla' \cdot q') \tag{39}$$

$$Q^* = \frac{1}{A'} \int_{A'} q'_s \, dA' \tag{40}$$

where we have defined the following dimensionless variables:

$$\begin{aligned} h &= h' h_a \\ t &= t' t_d \\ q &= q' p \ell_g \\ q_s &= q'_s p. \end{aligned} \tag{41}$$

Because runoff appears as a dimensionless parameter Q^* in the geomorphic equation, we are still able to obtain a parameterless expression for topographic evolution. There are, however, four dimensionless parameter groups that we cannot eliminate. Thus, in contrast to the *NoHyd* model, all solutions of the *DupuitLEM* model do not reduce to a single solution that can be rescaled to obtain all others. We will give the dimensionless groups the following names, which will be used throughout the rest of this paper:

$$\alpha = \frac{h_g}{\ell_g} = \frac{U}{v_0^{1/3} D^{1/3} K^{2/3}} \quad \text{Characteristic gradient} \tag{42}$$

$$\gamma = \frac{b}{h_a} = \frac{b k_s h_g}{p \ell_g^2} = \frac{b k_s U}{p D} \quad \text{Drainage capacity} \tag{43}$$

$$\mathrm{Hi} = \frac{h_g}{h_a} = \frac{k_s h_g^2}{p \ell_g^2} = \frac{k_s U^2}{p v_0^{2/3} D^{2/3} K^{4/3}} \quad \text{Hillslope number} \tag{44}$$

$$\delta = \frac{t_d}{t_g} = \frac{n_e v_0^{2/3} D^{2/3} K^{4/3}}{k_s U} \quad \text{Timescale factor} \tag{45}$$

Here α is a characteristic gradient of the model that emerges from the geomorphic parameters. The drainage capacity γ is proportional to the maximum transmissivity and the characteristic topographic gradient and inversely proportional to the mean recharge rate. Hi is analogous to the Hillslope number presented by Brutsaert (2005, their Equation 10.139) and used by Harman and Sivapalan (2009), Harman and Kim (2019), and others to understand shallow groundwater dynamics. Brutsaert (2005) and Berne et al. (2005) recognize that the Dupuit-Forcheimer model can be reduced to an advection-diffusion equation on aquifer thickness, in which advection corresponds

to flow driven by topographic gradients, and diffusion driven by gradients in aquifer thickness. As the factor 1/Hi = h_d/h_g appears as a coefficient on the diffusive term, Hi can be thought of as a Peclet number, in which large values correspond to flow primarily driven by advective forces, while small values correspond to flow primarily driven by diffusive forces (Berne et al., 2005). An analysis presented in Appendix B discusses the scaling properties of the governing equations in the special cases when Hi is small and large. Lastly, δ represents the scaling between the hydrologic and geomorphic timescales of the model. By the nature of hydrologic and geomorphic processes, we expect this ratio to be very small in all cases. Additionally, δ multiplies the time rate of change of aquifer thickness, which should also be very small here as we only consider steady recharge.

4.3. Predictions From Scaling Analysis

The scaling analysis will significantly improve our ability to explore and understand variability across the parameter space in the following sections. From the scaling analysis alone, we can make several predictions of what we expect to see in the numerical results. In particular, we expect to find the following at geomorphic steady state:

1. **Dimensionless topography from the *NoHyd* model should be identical, regardless of chosen h_g and ℓ_g.** If the boundary and initial conditions and the dimensionless domain size are the same, the absence of parameters in the dimensionless governing equations implies that the dimensionless topography should be invariant.
2. **Dimensionless topography from the *DupuitLEM* model should only be invariant to changes in h_g and ℓ_g when their ratio is held constant.** Because the *DupuitLEM* model retains a dependence on $\alpha = h_g/\ell_g$, the invariance found for the *NoHyd* model should only occur when we keep all dimensionless parameters the same, including α.
3. **Dimensionless topography should be insensitive to α when Hi is small.** In this case, relief is small relative to aquifer thickness, and we can neglect the role of topographic gradients in driving groundwater flow. We repeat the scaling analysis under these circumstances (Appendix B) and find that α does not appear.
4. **Dimensionless topography should be insensitive to Hi when Hi is large.** This case is the complement to the previous in that relief is generally large relative to aquifer thickness, and we can neglect the influence of gradients in aquifer thickness on groundwater flow. Again we repeat the scaling analysis under these circumstances (Appendix B) and find that Hi does not appear.

5. Results

We explore the properties of the scaled model through a series of simulations designed to sample the nondimensional parameter space of α, γ, and Hi. While the timescale parameter δ does vary as we vary hydrological parameters, this effect should be negligible for reasons previously stated. First, we test the predictions made from the scaling analysis through a series of simulations involving both the *NoHyd* model and the *DupuitLEM* model. Second, we use the *DupuitLEM* model to explore topographic and runoff variation with varying drainage capacity γ and hillslope number Hi.

We evaluated the condition of steady-state topography on the basis of change in mean dimensionless relief R_h/h_g, where R_h is the mean value of elevation z. For runs of the *NoHyd* model and runs of the *DupuitLEM* model where $\gamma < 1$, the results show clear indications of steady state, as the absolute value of dimensionless rate of relief change $|\frac{dR_h/hg}{dt/t_g}|$ declines below 10^{-10}. In cases with larger γ, perturbations continue through time in the absolute value of relief change. We run the model at least until there is no decreasing trend in the absolute value of relief change. Times to meet these conditions range from approximately 300–2,000 t_g (around 7–45 million years given the dimensional input parameters).

5.1. Confirmation of Scaling and Similarity

The numerical results confirm the predictions of our scaling analysis. Rows of Figure 2 labeled with capital letters correspond to the first three predictions in Section 4.3, while Figure 3 corresponds with the fourth prediction from Section 4.3.

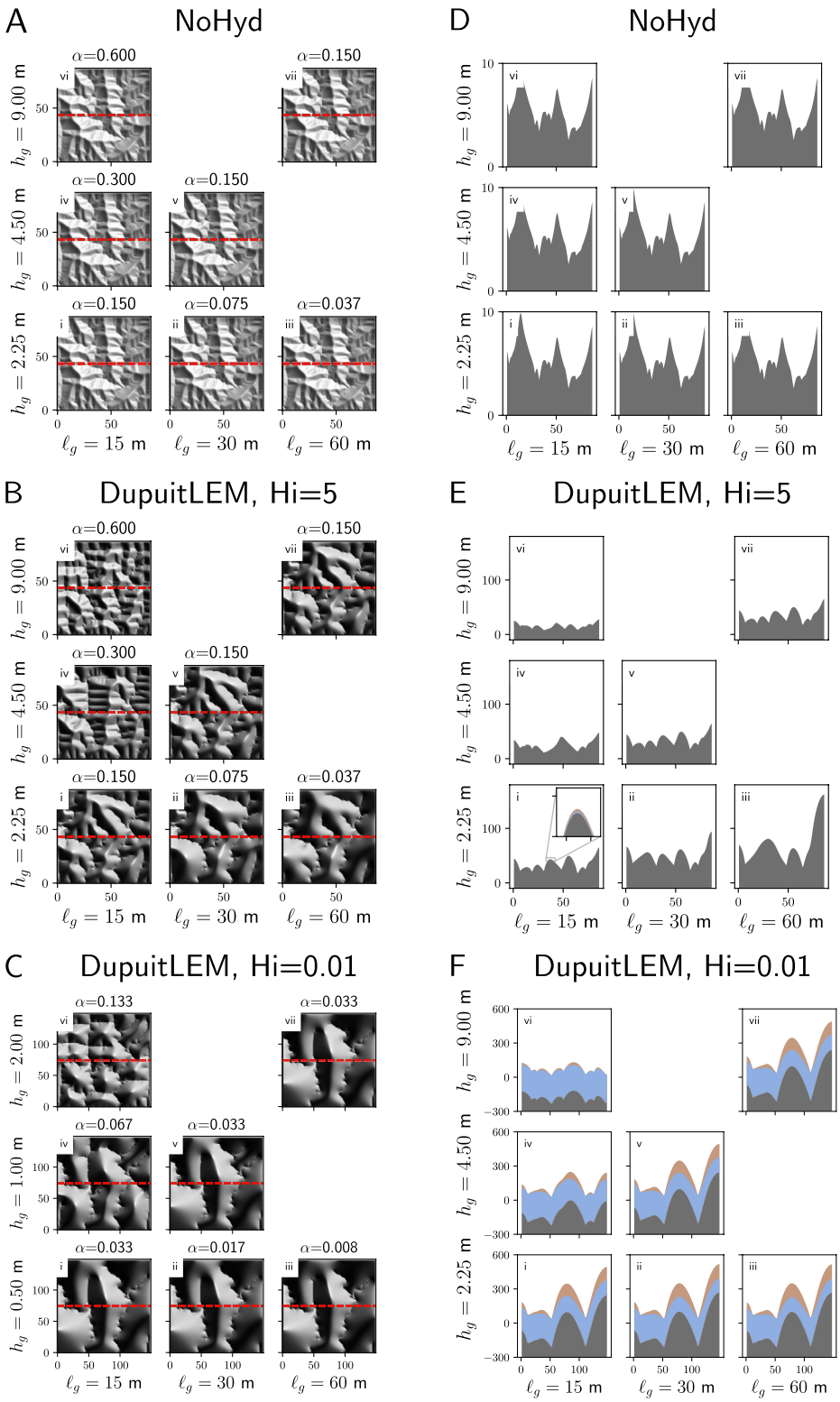
A
NoHyd
D
NoHyd
B
DupuitLEM, Hi=5
E
DupuitLEM, Hi=5
C
DupuitLEM, Hi=0.01
F
DupuitLEM, Hi=0.01
$\ell_g = 15$ m
$\ell_g = 30$ m
$\ell_g = 60$ m
$h_g = 9.00$ m
$h_g = 4.50$ m
$h_g = 2.25$ m
$h_g = 2.00$ m
$h_g = 1.00$ m
$h_g = 0.50$ m

Figure 2.

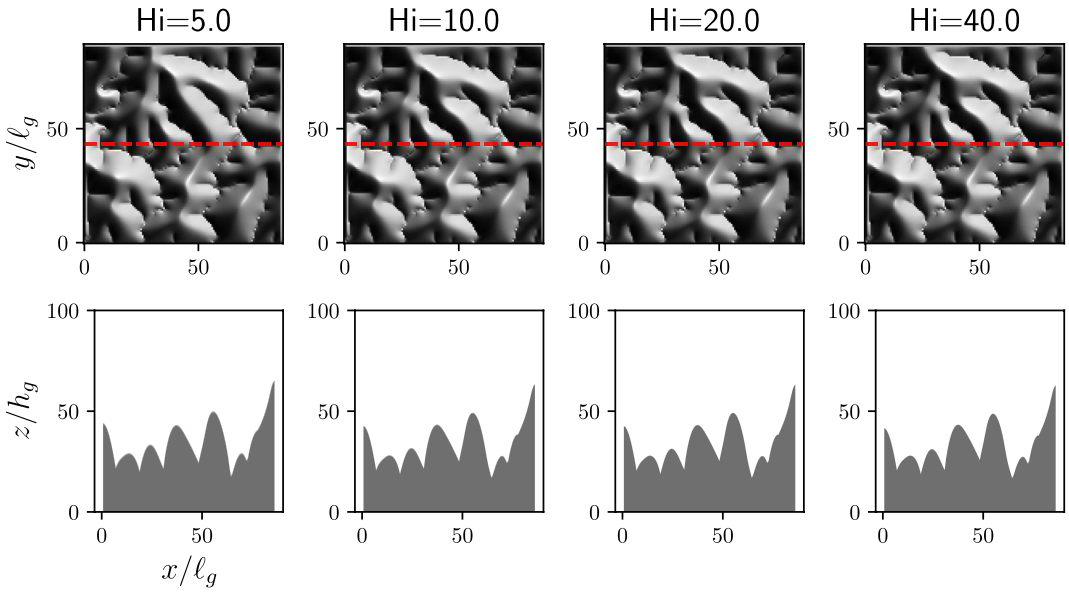

Figure 3. Hillshades and cross-sections of steady-state elevation from *DupuitLEM* for large values of Hi, with $\alpha = 0.15$ and $\gamma = 2.5$. Cross-sections are taken along the dashed red lines and domain scaled in same fashion as in Figure 2. Results confirm that model topography is insensitive to Hi at large values of Hi, as predicted by the scaling analysis.

Addressing the first scaling prediction, in Figures 2ai, 2aii, and 2aiii we show that ℓ_g can be varied independently from h_g (changing α) with the *NoHyd* model and we can still obtain visually and numerically identical results in the rescaled coordinate system (x', y', z'). The same similarity appears when h_g is varied independently while ℓ_g remains constant (i, iv, vi) and when h_g and ℓ_g are varied together (i, v, vii). The mean absolute difference in z' between all model runs is less than 10^{-13}% of total relief. These results confirm the scaling found by Theodoratos et al. (2018), showing that the vertical and horizontal dimensions possess distinct and independent scaling relationships.

Next we address the second scaling prediction that the vertical and horizontal length scales should not scale independently in *DupuitLEM*, unless Hi $\ll 1$. Figure 2b shows the same scaling of h_g and ℓ_g implemented in Figure 2a, now using *DupuitLEM* with a large hillslope number Hi = 5 and moderate drainage capacity $\gamma = 2.5$. As ℓ_g is increased independent of h_g (i, ii, iii), α decreases and the distance between channels appears to increase. Similarly as we increase h_g while holding ℓ_g constant (i, iv, vi), α increases and we observe a decrease in spacing between channels. These appear at first to be counterintuitive results: when relief is smaller, we might expect weaker topographic gradients driving groundwater flow, and therefore more surface runoff. However because we hold drainage capacity constant, we account for this effect. This is most clearly seen when we rewrite $\gamma = \frac{bk_s h_g/\ell_g}{p\ell_g}$, where the factor h_g/ℓ_g appears in the numerator. In other words, other terms in γ must be changed in order to keep the whole dimensionless group constant. On the other hand, consider where α appears in the dimensionless governing Equation 38 or alternatively Equation 39. These show that the dimensionless groundwater specific-discharge in fact has an inverse dependence on α^2: increasing α will lead to smaller dimensionless groundwater specific-discharge, and therefore more surface runoff. More intuitively, consider that the gradients driving flow and cross-sectional area through which flow moves downslope are both relative to the aquifer base.

Figure 2. Hillshade plots (a, b, and c) and cross-sections (d, e, and g) of steady-state elevation for model runs with varying h_g and ℓ_g. Cross-sections are taken along the dashed red lines and show the impermeable base elevation (dark gray), water-table elevation (blue), and topographic elevation (brown). Here zero elevation is the fixed topographic elevation boundary condition along the lower edge of the domain. Results are plotted in the rescaled coordinate system (x', y', z'). (a and d) Model runs with the *NoHyd* model, showing that topography is nearly identical in the dimensionless coordinate system regardless of the chosen values of h_g and ℓ_g. (b and e) *DupuitLEM* results are sensitive to independent scaling of ℓ_g ($i \rightarrow ii \rightarrow iii$) and h_g ($i \rightarrow iv \rightarrow vi$) when Hi is large. Scaling such that $\alpha = h_g/\ell_g$ remains constant produces topography that is similar in the rescaled coordinates. (c and f) *DupuitLEM* results with small Hi, showing reduced sensitivity of modeled topography to chosen length scales for small values of α. Note that the dimensionless size of the domain in the Hi = 0.01 cases is larger than the other cases in order to resolve a sufficient number of ridge-valley features. This was accomplished by maintaining the number of grid cells and increasing the contour width v_0. The values of h_g in the Hi = 0.01 cases (c and f) are also smaller to allow for achievement of a tractable solution with very small Hi.

Thus, increasing the slope and holding all other factors constant results in smaller gradients relative to the base, and smaller cross-sectional area through which the flow must move.

It is only when h_g and ℓ_g are varied together (i, v, vii), keeping α constant, that topography remains invariant in the rescaled coordinates. The greatest difference in mean relief between runs is 0.20%. While sufficient to confirm the scaling analysis, this difference is larger to that observed in Figure 2A due to isolated areas that develop slightly different drainage patterns. This is likely as a result of small numerical differences between the groundwater model solutions early in the evolution of topography.

Third, we address the scaling prediction that when the hillslope number Hi is small, vertical and horizontal dimensions should scale independently, and thus the dimensionless results should be independent of the characteristic gradient α. When Hi is small, relief is small relative to the characteristic aquifer thickness, and as a result relief should not play a strong role in generating hydraulic gradients that drive flow. In these simulations where permeable thickness is particularly deep relative to the domain size, we caution that the Dupuit-Forcheimer solution may be significantly different from an equivalent 3-dimensional flow solution. Figure 2c shows the results of varying h_g and ℓ_g as in Figure 2b, but now with Hi = 0.01. Here we find less dependency of the results on α than when Hi = 5.0, particularly when $\alpha < 0.05$. Plots (i, iv, vi) show reduced dependency on α, with a maximum 51% difference in mean relief, in comparison to 145% difference when Hi = 5.0. There is less variation in plots (i, ii, iii), with 3.9% difference in mean relief, in comparison to 87% difference in mean relief when Hi = 5.0. This partially confirms what we expect from the scaling analysis, but suggests some additional dependency on α or h_g.

Last, we address the scaling prediction that when the hillslope number Hi is large, the topography should not be sensitive to Hi. In this case, hydraulic gradients are primarily driven by topographic gradients, and Hi no longer appears in the dimensionless governing equations. Figure 3 shows results with increasing Hi, with $\alpha = 0.15$ and $\gamma = 2.5$ in all cases. Topography is visually and numerically similar. The difference in mean relief between cases when Hi = 20.0 and Hi = 40.0 is 0.7%. These results demonstrate the efficacy of our scaling analysis. However in the results going forward, we will generally work with values of Hi in between those tested in the special cases here, and thus we will not be able to neglect α or Hi.

5.2. Sensitivity to Dimensionless Hydrologic Parameters

Varying the drainage capacity γ and hillslope number Hi in the numerical simulations suggests that landscape and climate properties affecting shallow groundwater flow have major effects on topography. In particular, the evolved topography depends strongly on γ, where low γ correlates with low transmissivity, and a characteristic aquifer thickness that is large relative to permeable thickness. When $\gamma = 0.5$, the lowest value shown in Figure 4, the results look very similar to those obtained with the *NoHyd* model. In these cases the entire landscape experiences some overland flow and erosion, which is apparent in the spatial distribution of runoff Q^* shown in Figure 6. In contrast, high γ cases produce broad interfluves on which $Q^* = 0$, as the water table sits further below the surface. As a result these areas do not experience surface erosion. To a lesser degree, the hillslope number affects the steady-state topography as well, where increasing hillslope number increases the degree to which topographic gradients, rather than gradients in aquifer thickness, drive groundwater flow. Here we increase Hi by increasing the hydraulic conductivity, while decreasing permeable thickness b in order to hold the drainage capacity γ constant. The cross-section plots in Figure 5 confirm that permeable thickness is larger when Hi is small. The topographic effect of this difference in permeable thickness appears to be greatest when drainage capacity is large, suggesting that there is an interaction between the two parameters. In large drainage capacity cases, increasing Hi generally decreases the spacing between channels.

Distributions of Q^* represent the spatial variability in runoff that emerges from our coupled geomorphic-hydrologic model under conditions of steady, uniform recharge. These distributions confirm that the extent of areas contributing runoff tends to decrease with increasing drainage capacity, and to a lesser extent with decreasing hillslope number. Figure 6b shows cumulative distribution functions of Q^* for each model run, indicating the proportion of the landscape where Q^* is less than a particular value on the x-axis. Strikingly, we see that areas that contribute no runoff ($Q^* = 0$) first appear exactly when $\gamma = 1$ (third row from the bottom). This holds for smaller and larger values of α as well (see Figures S3 and S6 in Supporting Information S1). It is at this point that the spatial variability in Q^* is maximized: at lower values all areas contribute some runoff, while above this value, most areas contribute no runoff at all. As γ is the ratio of the characteristic aquifer thickness h_a to the permeable thickness

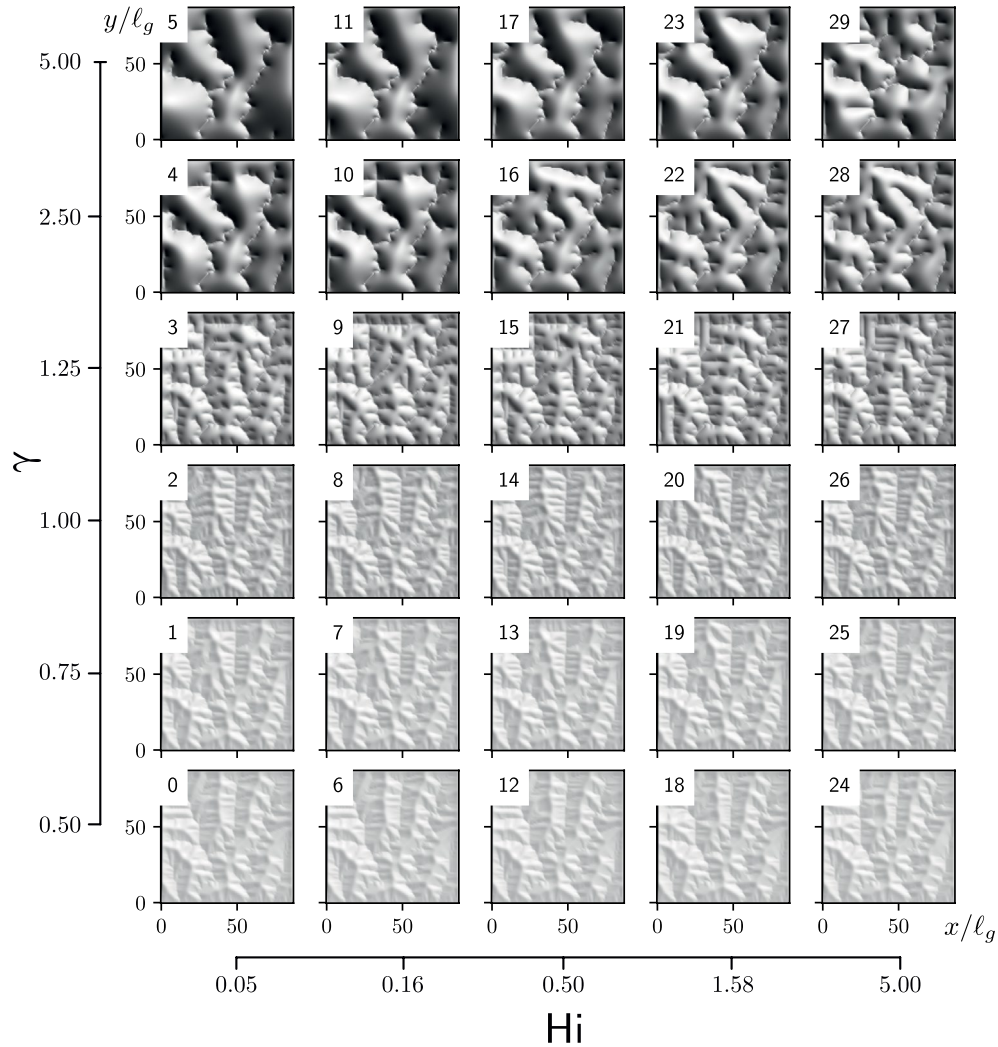

Figure 4. Hillshade plots of steady-state elevation using *DupuitLEM*, varying γ and Hi while α is held constant. Hi varies over two orders of magnitude on a geometric scale, while γ varies over one order of magnitude, further subdivided to show the transition that occurs at $\gamma = 1$. Low γ topography appears similar to *NoHyd* model results, and is less sensitive to varying Hi. Large γ results show broad hillslopes and slightly greater sensitivity to Hi.

b, a value of 1 should indicate that a "characteristic hillslope" has just become saturated, which appears to be in agreement with our results. This is a powerful demonstration of the effectiveness of this nondimensionalization.

In Figure 6c, the proportion of numerical grid nodes with a dimensionless runoff rate $Q^* > 0.5$ indicates extensive saturation in low γ cases with minor sensitivity to Hi values; the extent of runoff contributing areas declines slightly more rapidly when Hi is large. For comparison, we also plot the proportion of the landscape with positive curvature, which shows a more gradual change with γ.

The previous section evaluating the scaling properties of the model results showed that the characteristic gradient α has a significant effect on topography in most cases where Hi is not very small. Supporting Information S1 includes figures showing the results of varying γ and Hi with higher and lower values of α than those shown here. While the results for large drainage capacity do show some differences, the fundamental patterns seen, including transitions in morphology and runoff generation at $\gamma = 1$, remain the same.

These results demonstrate that subsurface hydrology has a strong effect on topography in this model. In particular we find that $\gamma = 1$ defines the transition between two landscape behaviors. When $\gamma < 1$, landscapes evolve with

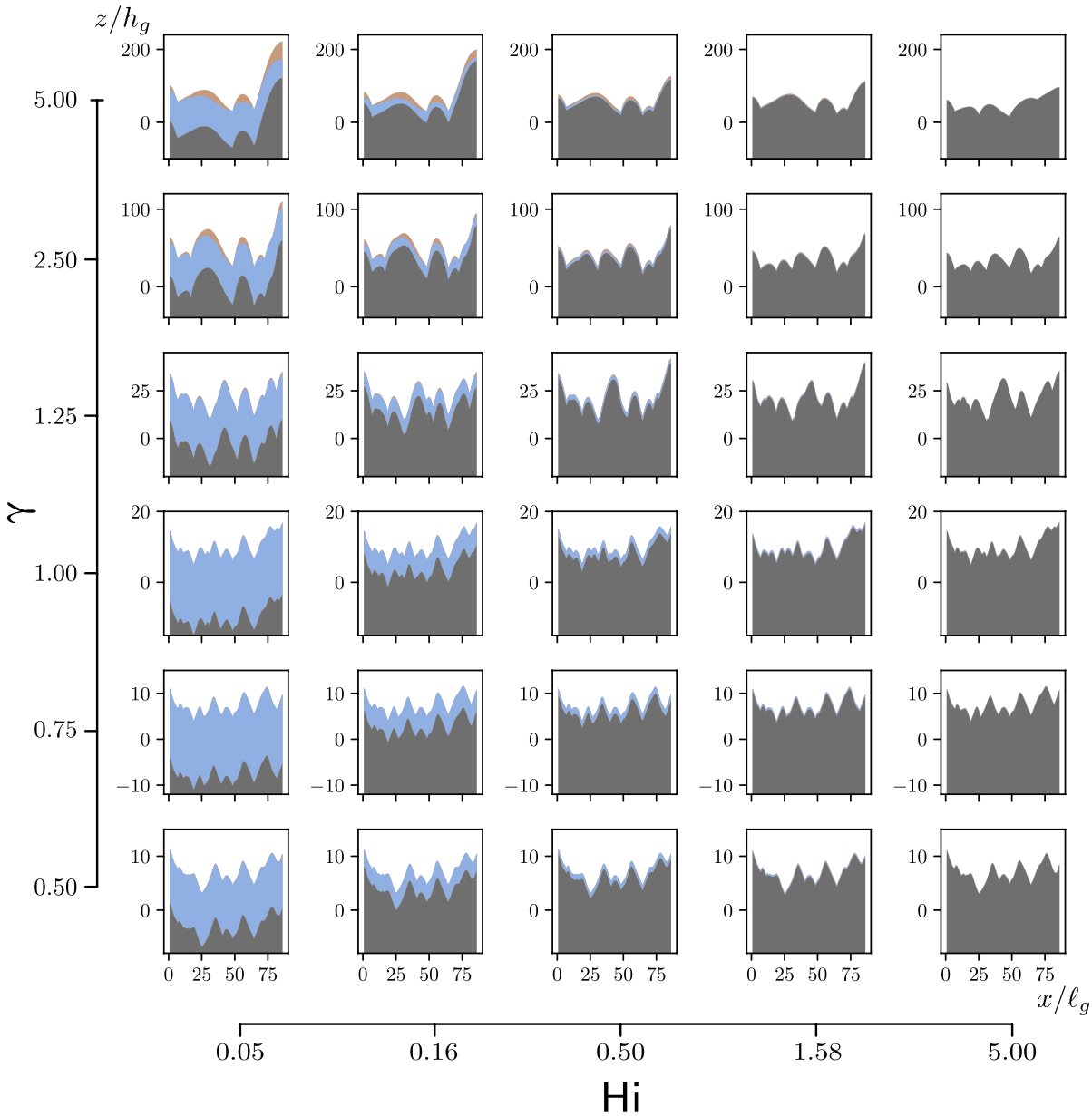

Figure 5. Cross-section plots of *DupuitLEM* results with varying γ and Hi corresponding to hillshades in Figure 4. Cross-sections are taken in the same fashion as Figure 2, horizontally along the midpoint of the domain. Despite apparent similarities of the hillshades, there are prominent differences in the subsurface with varying Hi. Lower Hi cases will have deeper regolith, as this is dependent on the value of Hi. Noticeable depth to water table only becomes apparent at large values of γ.

close spacing between channels, low relief, and extensive saturation and runoff generation. When $\gamma > 1$, water is increasingly partitioned toward subsurface rather than surface flow. Consequently, the spacing between streams is greater, the landscape is generally steeper, and saturated areas and erosion are restricted to narrow incised regions.

6. Emergent Properties at Landscape Equilibrium

6.1. Topographic Analysis: Steepness and Curvature

The landscapes shown in Figures 2, 4, and 6 reveal the visually striking influence of hydrological properties on landscape form. However, there is still much more we can learn about the controls on these emergent properties, guided by the form of the governing equations. Furthermore, we would like to be able to develop some quantitative understanding that relates readily observable topographic features to hydrological properties that are more

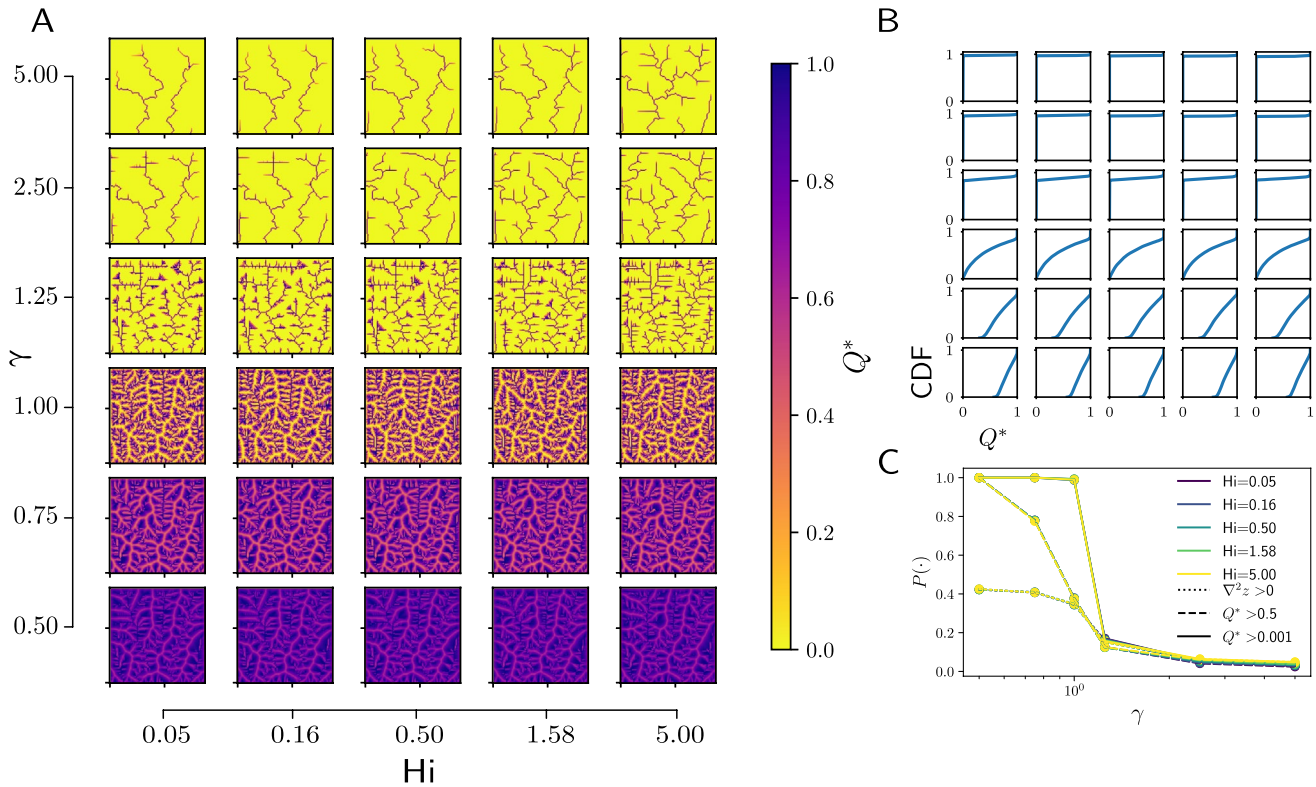

Figure 6. (a) Spatial patterns of Q^* from *DupuitLEM* varying γ and Hi while all other parameters are held constant. Results are similar across differences in Hi, but show significant differences with γ. All points in the landscape generate some runoff in the lowest *gamma* trials. (b) Cumulative distribution functions of Q^* with varying γ and Hi. Low γ trials show a range of Q^* values, with all areas contributing to some degree. High γ cases show that most areas do not contribute runoff, with a small area where $Q^* \approx 1$. (c) Proportion of nodes contributing runoff or having positive curvature, with varying γ (x-axis) and Hi (colors). Results show decreasing proportion of total area that is contributing runoff or is convex with increasing γ.

difficult to measure. The relationships between model parameters and emergent hydrologic and geomorphic properties will be the focus of this section.

Commonly, properties of stream channels and entire landscapes are examined by plotting local slope versus upslope area (e.g., Dietrich et al., 1993; Tarboton et al., 1989; Willgoose et al., 1991c). Results form point clouds where zones of distinct behavior can be identified (Perron et al., 2008). Recently, Theodoratos et al. (2018) showed that the topography resulting from the streampower-linear diffusion LEM may be analyzed by examining relationships between what they term the incision height $\sqrt{A}|\nabla z|$ and Laplacian curvature $\nabla^2 z$. Theodoratos and Kirchner, 2020b refer to $\sqrt{A}|\nabla z|$ as steepness, so here we will adopt similar terminology, with one difference: to match the form of our governing equations, we define steepness as $\sqrt{a}|\nabla z|$, using area per contour width a rather than area A. Steepness and curvature emerge naturally from the steady-state form of the governing equation for topographic evolution (Equation 20). Setting the time rate of change equal to zero, and rearranging, we obtain the following relationship:

$$\nabla^2 z = \ell_g^{-3/2} Q^* \sqrt{a}|\nabla z| - \frac{h_g}{\ell_g^2} \tag{46}$$

which has the equivalent dimensionless form:

$$\nabla'^2 z' = Q^* \sqrt{a'}|\nabla' z'| - 1 \tag{47}$$

When runoff generation is spatially uniform, as in the *NoHyd* model, $Q^* = 1$ for all (x, y) and there is a linear relationship between steepness and curvature, with a slope of unity and intercept of -1 in dimensionless coordinates, as observed by Theodoratos et al. (2018). While this definition of steepness is contingent on the particular

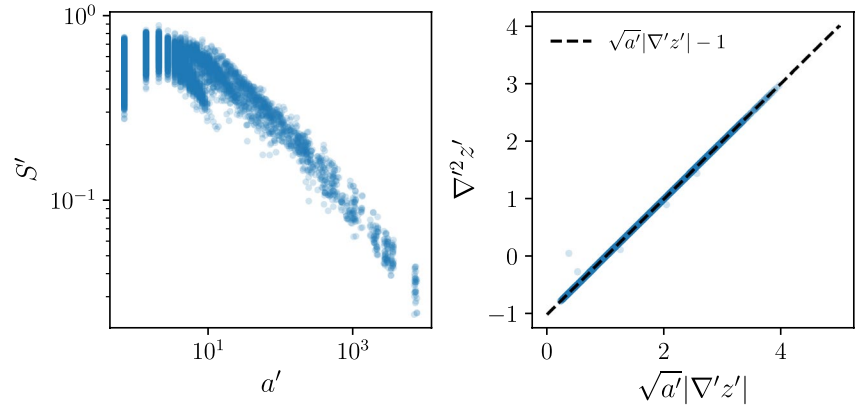

Figure 7. Dimensionless slope-area (left) and steepness-curvature plots (right) of steady-state topography using the *NoHyd* model. The steepness-curvature relationship observed in the results shows a precise fit to the linear relationship predicted from theory (dotted line). Parameters selected are the same as those in Figure 2ai.

exponents on area and slope, Theodoratos et al. (2018) showed that this relationship can be generalized to any exponent values, albeit with significantly more complicated formulas.

Figure 7 shows topography from a run of the *NoHyd* model in slope-area and steepness-curvature space. The results show the expected slope and intercept in the steepness-curvature plot. All of the variability that appears in the slope-area space collapses onto a single line in steepness-curvature space, making steepness-curvature plots powerful tools for examining model behavior. Observing this relationship in the numerical solution also demonstrates that the model accurately reproduces the analytical result at steady state.

Furthermore, deviations created by the introduction of hydrologic variability with Q^* should be readily apparent when plotting steepness versus curvature. When we use *DupuitLEM*, plotting $Q^*\sqrt{a'}|\nabla' z'|$ rather than $\sqrt{a'}|\nabla' z'|$ versus curvature would again result in a linear relationship. Through topographic analysis alone, however, steepness and curvature are available while Q^* is not. Quantifying the relationship between these topographically derived quantities and Q^* across each steady-state landscape in our nondimensional parameter space thus supports quantifying hydrological function based upon topography.

Slope-area and steepness-curvature plots for selected model runs with different values of drainage capacity γ and hillslope number Hi are shown in Figure 8. The steepness-curvature relationships when drainage capacity is small show close agreement with the theoretical relationships derived from the *NoHyd* model (dotted black line). This is consistent with the observed values of Q^*, which are close to unity at most nodes. With increasing drainage capacity, there is an apparent separation between points that conform to the theoretical relationship and points that maintain constant negative curvature $\nabla^2 z = -h_g/\ell_g^2$. The difference between these behaviors is revealed in the values of Q^*. Areas in yellow have $Q^* \approx 0$, and form the zone of constant negative curvature. This is exactly what we would expect from the solution to the steady-state Equation 47 in the absence of the fluvial incision term. Points in this zone are convex hillslopes that do not reach surface saturation. Areas in blue have $Q^* \approx 1$, essentially conforming to the same relationship observed for the *NoHyd* model. Points in this zone are the fluvial valleys that are fully saturated and have discharge approximately equal to the recharge rate integrates over the upslope area. This indicates that the vast majority of water is moving over the surface rather than through the subsurface at these locations. A limited number of nodes fall in between these two end members of behavior. These are the channel heads and other areas of partial runoff contribution, where $0 < Q^* < 1$. The proportion of points in this intermediate space appears to decrease with increasing γ.

Slope-area plots show separation between these behaviors as well, though the end members of behavior are not nearly as distinct, nor can we explain their patterns as readily from the analytical solution to the governing equations at steady state. Differences between channel and hillslope morphology are also apparent in map view plots of steepness and curvature (Figure 9). While steepness does seem to provide an indication of increasing channelization in the low drainage capacity cases, in the high drainage capacity cases, it takes on unusual swirling patterns on hillslopes, in part due to the D8 flow routing method. These are of little consequence in the context

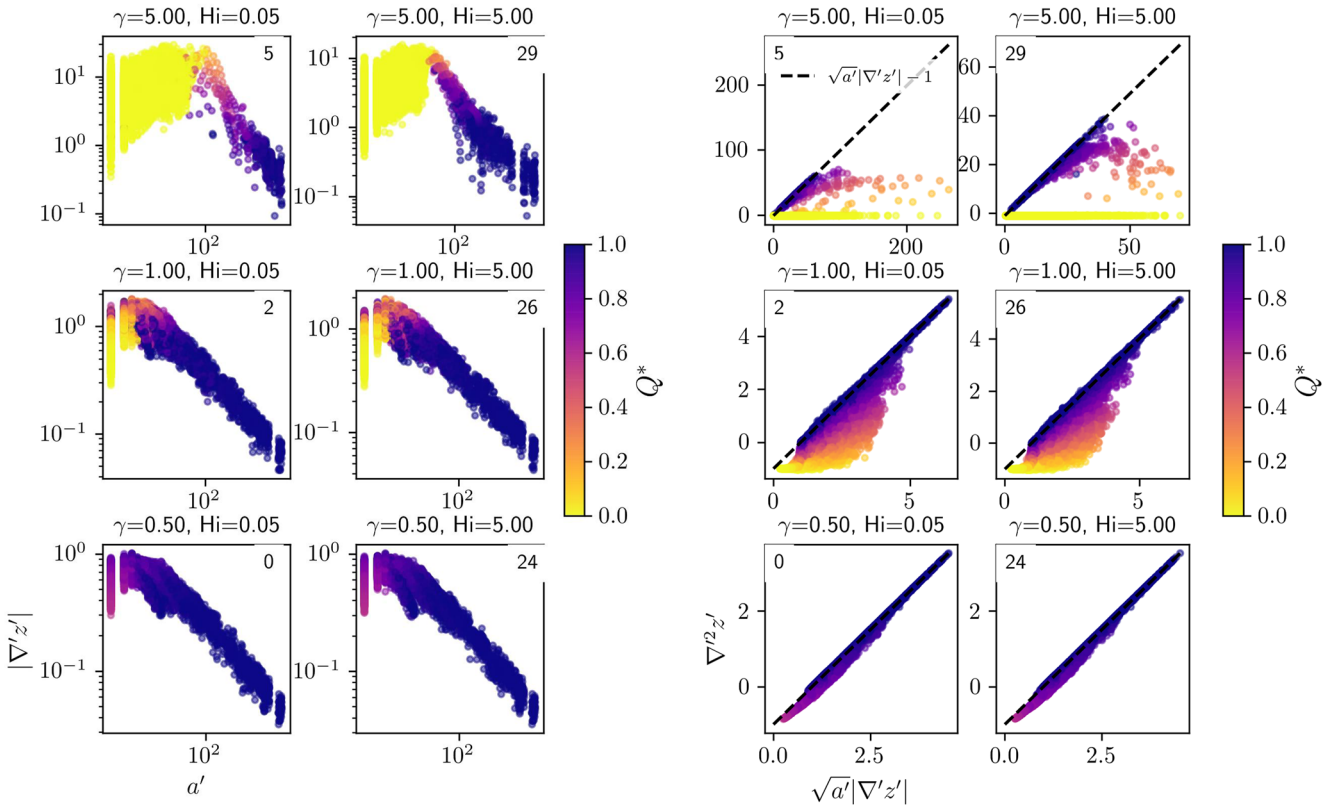

Figure 8. Dimensionless slope-area (left) and steepness-curvature (right) plots for selected model runs from Figure 4. See correlating model run numbers in the upper left corner. As in Figure 4, γ and Hi increase vertically and laterally from the bottom left respectively. Plots are colored by Q^* of the final topography. Axes scales are different between plots, showing that large γ cases obtain values of dimensionless steepness and curvature far greater than the cases when γ is small.

of processes acting in the model, because Q^* and therefore fluvial incision are near zero on these hillslopes. In low drainage capacity cases, map view curvature plots show that areas of negative curvature are restricted to narrow areas near the ridges, while extensive areas have near zero or positive curvatures, indicating predominantly concave-upward terrain. In comparison, in high drainage capacity cases, most points obtain a constant negative curvature, representing convex-upward hillslopes, while the channels obtain large positive curvatures as a consequence of the steep adjacent hillslopes.

6.2. Hydromorphic Balance

How can we understand the separation between channel and hillslope behavior that appears in the *DupuitLEM* results? While there is a unique relationship between steepness and curvature for the *NoHyd* model, this is no longer the case for *DupuitLEM*, indicating that some information is not captured by these terms alone. The missing piece, as Equation 47 shows, is Q^*. That is, there is a unique relationship between steepness, curvature, and Q^*. If we would like to know Q^*, one approach would be to solve for Q^* and explore how it could be determined from the governing equations. Using the equation for topography at steady state (Equation 20), we can solve for Q^* as a function of the parameters, steepness, and curvature.

$$Q^* = \ell_g^{3/2} \frac{\nabla^2 z}{\sqrt{a}|\nabla z|} + \frac{h_g}{\sqrt{\ell_g}} \frac{1}{\sqrt{a}|\nabla z|} \tag{48}$$

We will call this equation the *Geomorphic Balance*. Results of plotting Q^* versus the right hand side of this equation are shown in Figure 11a. Like the relationship between steepness and curvature for the *NoHyd* model, the *Geomorphic Balance* shows a tight linear relationship. In other words, most places in the landscape have topography that is closely coupled with runoff, as predicted by the governing equations. Deviation from the 1:1

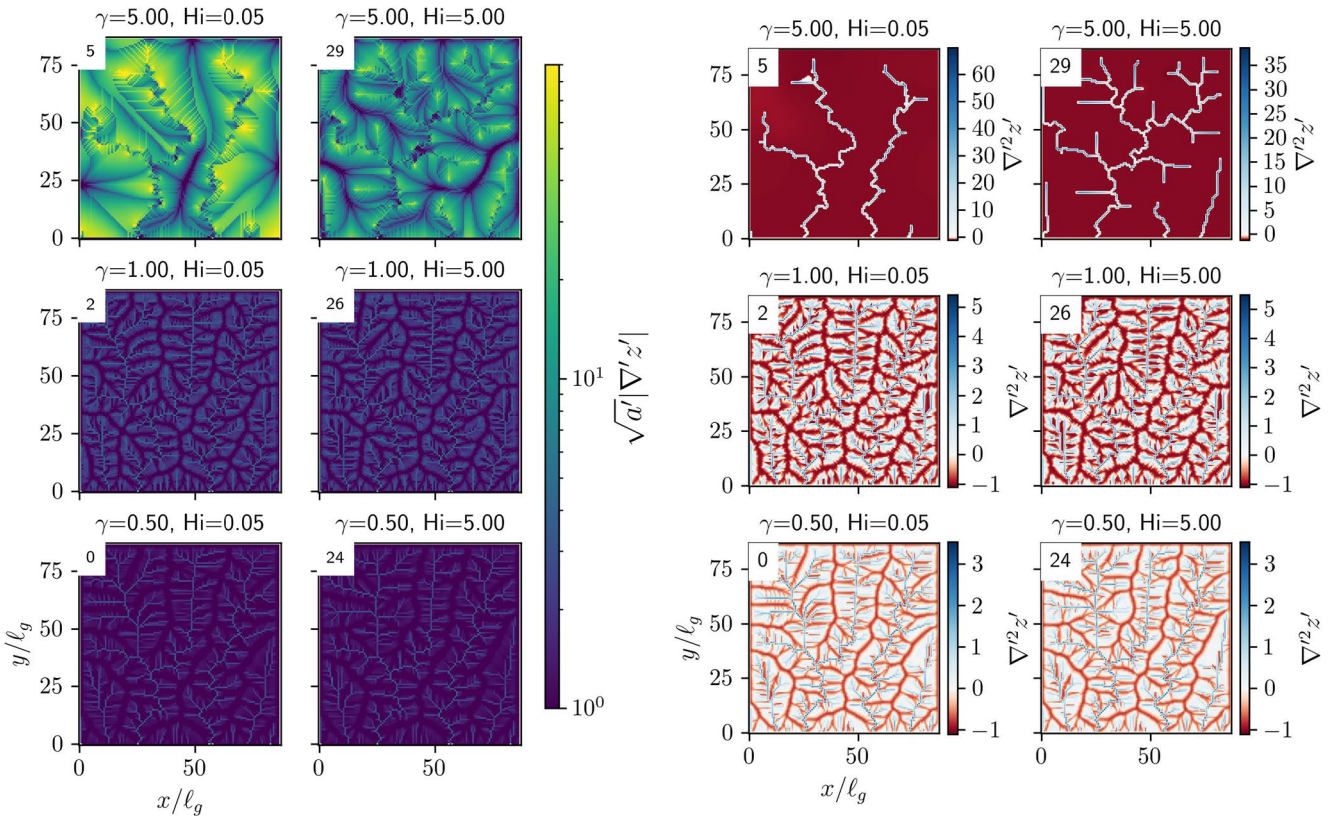

Figure 9. Planform view steepness and curvature for selected model runs, with model run numbers corresponding to hillshades in Figure 4. Spatial patterns of steepness appear to agree with channel network locations in the low γ cases, while in the high γ cases, steepness takes on large values in patterns that spiral away from ridges. Curvature is positive on ridges and negative in channels, with large areas of constant negative curvature in the large γ cases.

line in Figure 11a is an indication that the hydrologic state and geomorphic state are not completely in equilibrium with one another. These deviations likely have a similar origin to the perturbations in relief as the model evolves toward topographic steady state that we noted previously. Both indicate that subtle adjustments between the hydrologic and geomorphic states persist in the evolution of the modeled landscapes. This demonstration of dynamic equilibrium has similarities to natural settings where adjustment to small perturbations is persistent even in landscapes that are considered to be near geomorphic steady state.

Unfortunately in most cases where one might want to apply the *Geomorphic Balance* to real data to determine spatial patterns of runoff and saturation, the geomorphic length scales h_g and ℓ_g are unknown. While the *NoHyd* model has distinct relationships between landscape properties and h_g and ℓ_g, explored by Theodoratos et al. (2018), those relationships break down with the addition of subsurface hydrology. Even if we were to estimate h_g and ℓ_g through geomorphic methods, the uncertainty in direct estimates these parameters is likely far too great to constrain Q^* in Equation 48.

The governing hydrologic equations offer a complementary solution for Q^*. At hydrological steady state, for steady recharge at rate p, the expression for conservation of mass (Equation 16) can be written as:

$$p = \nabla \cdot q + q_s \tag{49}$$

This should be a reasonable representation of our results, as the recharge rate is constant, and other properties vary slowly with time. Integrating this water balance over the watershed area, A, and using Leibniz' rule to evaluate the integral of the divergence term:

$$\int_A p \; dA = \int_A (\nabla \cdot q + q_s) \; dA \tag{50}$$

$$pA = \iint \nabla \cdot q \, dx dy + Q^* pA \tag{51}$$

$$pA = \oint_S q \cdot \hat{n} \, dS + Q^* pA \tag{52}$$

where S is the catchment boundary and $\hat{n}$ is the unit normal vector on the catchment boundary. If we assume that the catchment boundary is a no-flux boundary except for the outlet with characteristic contour width v_0, then this reduces to:

$$pA = qv_0 + Q^* pA \tag{53}$$

This also assumes that groundwater flux is directed out of the watershed, which is a tenuous assumption for deeper regional aquifers but perhaps is appropriate for the shallow near surface aquifers that tend to produce return flow and near-channel areas of surface saturation during rainfall events. We selected the characteristic contour width v_0 here to be the same as the contour width used in Equation 8, so the relationship $A = v_0 a$ still holds. Next we substitute the expression for groundwater flow (Equation 17). Assuming gradients are directed out of the watershed, we can take the absolute value of gradients for similarity to the geomorphic balance.

$$pA = v_0 k_s h(|\nabla h| + |\nabla z|)\cos^2(\theta) + Q^* pA \tag{54}$$

then substituting $A = av_0$ and rearranging to solve for Q^*:

$$Q^* = 1 - \frac{k_s h}{p} \frac{(|\nabla h| + |\nabla z|)\cos^2(\theta)}{a} \tag{55}$$

By limiting ourselves to locations where the water table has reached the land surface so that the aquifer base and land surface are parallel, we can set $h \to b$ and $\nabla h \to 0$.

$$Q^* = 1 - \frac{k_s b}{p} \frac{|\nabla z|\cos^2(\theta)}{a} \tag{56}$$

This is our *Hydrologic Balance* expression for Q^*. Contained in this expression is a modified version of the topographic index $\frac{a}{\nabla z \cos^2(\theta)}$, where we have retained the cosine term for similarity to the governing equation for groundwater flow. It is appropriate that topographic index should appear in this equation, as it has been shown to be a useful tool for understanding geomorphically driven hydrological behavior (Beven & Kirkby, 1979). The results of plotting Q^* against the right hand side of Equation 56 are shown in Figure 11b. Correlations are not as strong as in the *Geomorphic Balance*.

Investigation revealed that differences between modeled results and our analytical solution result from differences in the style of surface versus subsurface flow routing. Subsurface flow is calculated in a "diffusive" sense by measuring fluxes in or out on all links connecting nodes of the computational mesh. In contrast, surface routing is calculated with an "advective," steepest descent approach, where all flow is routed downslope from one single node to another. The analytical solution assumes that the recharge on the upslope area, which we calculate with the "advective" method, is the total flow that is partitioned between surface and subsurface flow at a node. If all flow were routed with the "advective" method, we would expect the modified topographic index to have a 1:1 correspondence with Q^*. However, Figure 10 (right panel) shows that there is not a unique relationship between the two, particularly for small and intermediate values of topographic index. However, curvature (colors), which better captures the degree of landscape convergence or divergence driving groundwater flow, is able to explain the trend in Q^* at a given value of topographic index. While this pattern appears here as a consequence of our model choice, it may capture something intrinsic about reality in which surface flow is rapid and generally channelized in a single direction, while groundwater flow is more gradual and diffusive in nature. With two expressions for Q^*, one hydrologic in Equation 56 and one geomorphic in Equation 48, we can nevertheless continue our analysis, combining these expressions by eliminating Q^* to obtain:

$$1 - \frac{bk_s}{p} \frac{|\nabla z|\cos^2(\theta)}{a} = \ell_g^{3/2} \frac{\nabla^2 z}{\sqrt{a}|\nabla z|} + \frac{h_g}{\sqrt{\ell_g}} \frac{1}{\sqrt{a}|\nabla z|} \tag{57}$$

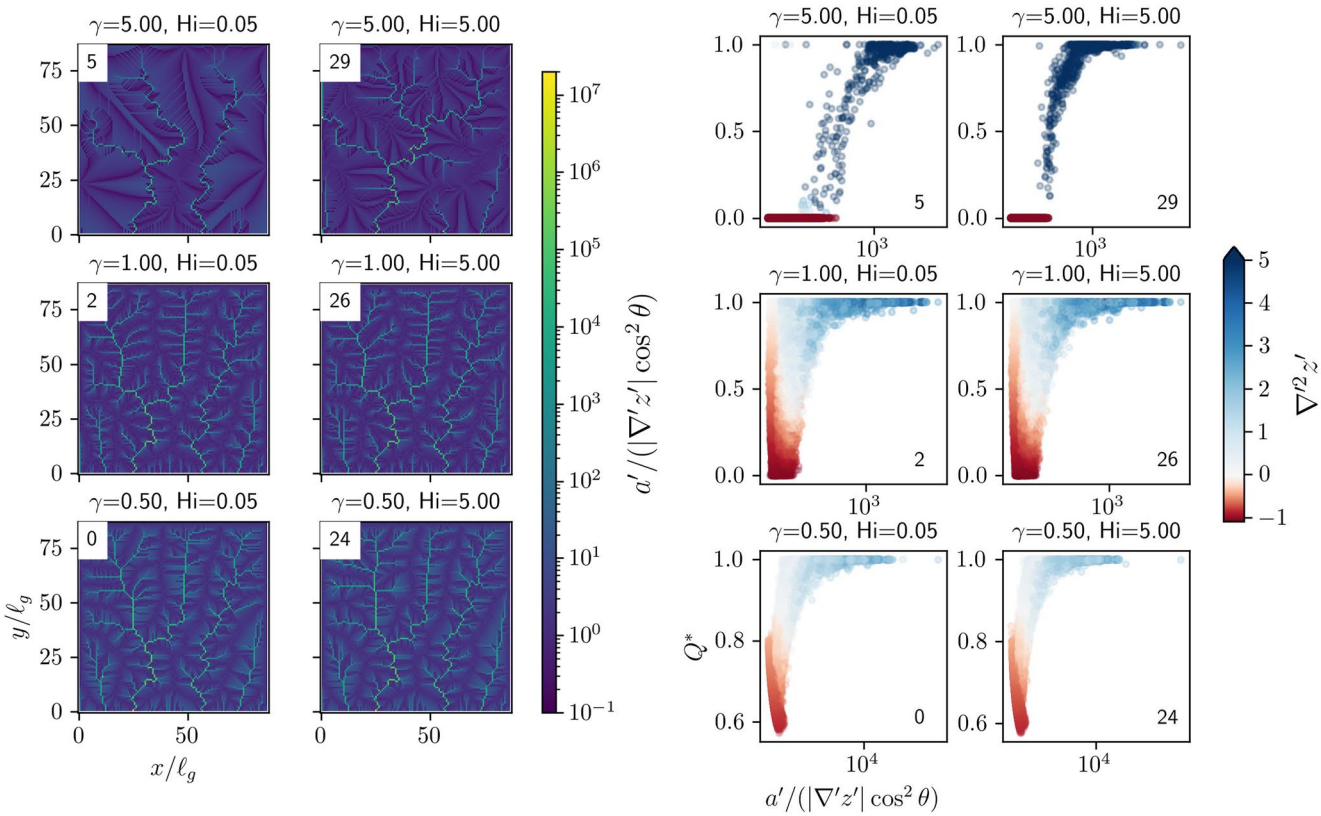

Figure 10. Planform view topographic index (left) and topographic index-Q^* relationship for selected model runs, with run number corresponding to hillshades in Figure 4. Coloring in the right panel reveals that curvature explains variation in Q^* at a given topographic index.

or equivalently:

$$0 = \frac{bk_s}{p}\left(\frac{|\nabla z|\cos^2(\theta)}{a}\right) + \ell_g^{3/2}\left(\frac{\nabla^2 z}{\sqrt{a}|\nabla z|}\right) + \frac{h_g}{\sqrt{\ell_g}}\left(\frac{1}{\sqrt{a}|\nabla z|}\right) - 1 \tag{58}$$

We call this expression the *Hydromorphic Balance*. It describes a fundamental relationship between steepness, curvature, and topographic index that emerges from the governing equations. Using the same nondimensionalization as previously, Equation 58 can be rewritten as:

$$0 = \gamma\frac{a'}{\nabla' z' \cos^2(\theta)} + \frac{\nabla'^2 z'}{\sqrt{a'}|\nabla' z'|} + \frac{1}{\sqrt{a'}|\nabla' z'|} - 1 \tag{59}$$

This relationship is the expanded equivalent of the linear relationship between steepness and curvature shown in the *NoHyd* model case, where an additional dimension, the modified topographic index, is needed to capture the effects of runoff generation from saturation excess overland flow. Figure 12 shows the hydromorphic balance relationship (transparent gray surface) and modeled topography (points colored by Q^*) for three cases: the *NoHyd* model case (A), a low drainage capacity case (B), and a high drainage capacity case (C). Recall that the *NoHyd* model effectively has a drainage capacity of zero, as all precipitation becomes surface runoff. We plot the log of the modified topographic index to improve readability of the figure and to be consistent with the conventional definition of topographic index (Beven & Kirkby, 1979). In the *NoHyd* case, all points fall on a plane that collapses to a line in steepness and curvature space. At higher subsurface capacity, places with lower topographic index (places less likely to contribute runoff) have lower curvature, as predicted by the *Hydromorphic Balance*. Locations where there is no surface runoff ($Q^* = 0$) do not fall on the surface, as the *Hydromorphic Balance* was only derived for locations where $Q^* > 0$.

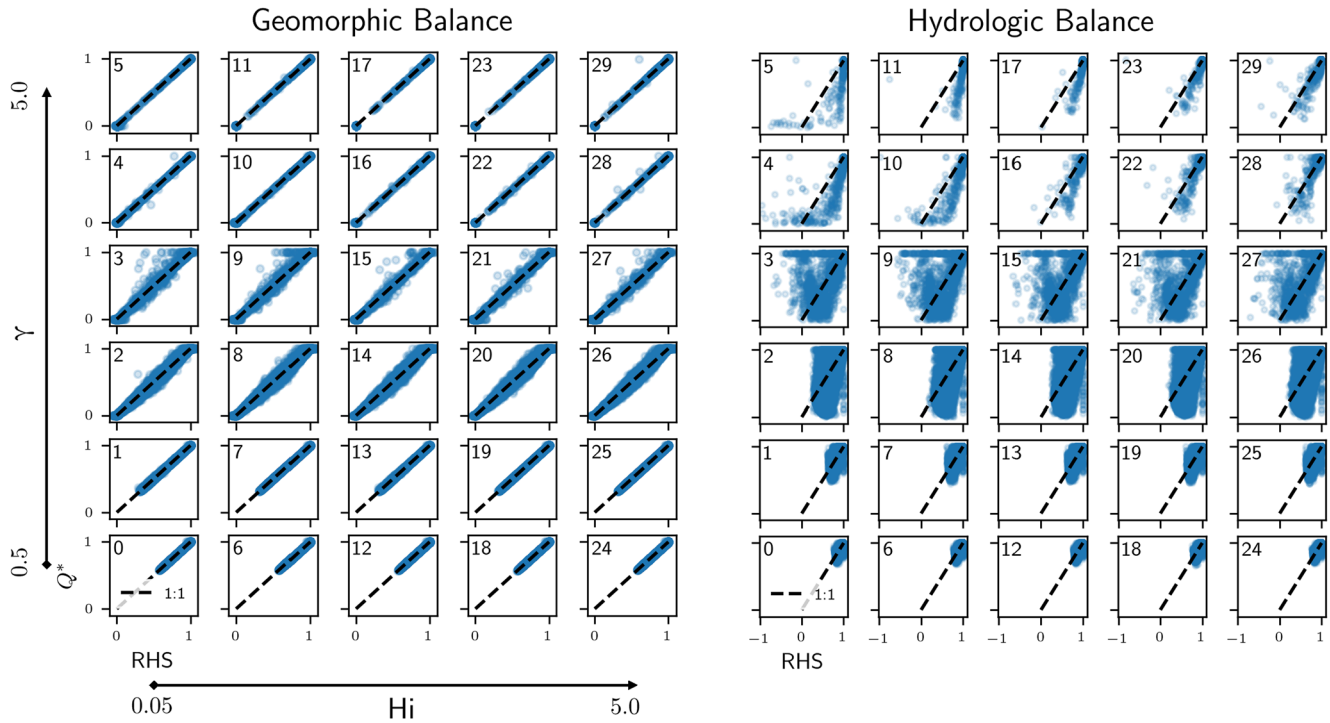

Figure 11. (a) Geomorphic balance from Equation 48, plotting Q^* against the right hand side (RHS) of the equation. Subplots correspond to the same model runs as in 4. (b) Hydrologic balance from Equation 56, plotting Q^* against the right hand side of the equation.

While there may be limitations to the application of the *Hydromorphic Balance* for quantitative terrain analysis (for example, estimating the transmissivity bk_s, which appears as a coefficient in Equation 58), it nonetheless has explanatory power for topography observed in our numerical simulations. Careful application to real data sets could provide evidence supporting the importance of subsurface flow processes for runoff generation and landscape evolution.

6.3. Emergent Hillslope Length

It is visually apparent in our results that emergent length scales of the ridge-valley topography increase with drainage capacity. This can be quantified by measuring and comparing the average hillslope length L_h across the parameter space. Here, we define L_h as the mean distance from hillslope points to the nearest channel. This is inversely proportional to twice the drainage density, where drainage density is calculated with the method described by Tucker et al. (2001). Hillslope length is of particular interest in the context of hydraulic groundwater theory, where it is an important control on both hillslope storage and characteristic response time (Harman & Sivapalan, 2009; Troch et al., 2003). In order to determine hillslope length, channel locations must be delimited. While it is common to use threshold values of steepness index to identify channels (e.g., Tucker et al., 2001), this implicitly assumes a relationship between steepness and incision, which is not necessarily the case in our model. Instead, we identify channels as points with positive Laplacian curvature ($\nabla^2 z > 0$), where fluvial incision is the dominant geomorphic process.

We can use the hydromorphic balance to predict the scaling relationship between hillslope length and the drainage capacity γ. We begin with the *Hydrologic* and *Geomorphic Balance* expressions, Equations 56 and 48. This time, rather than combining to eliminate Q^* as we did previously, we can combine to eliminate the topographic gradient $|\nabla z|$. Since we have defined channels as places where $\nabla^2 z > 0$, channel heads can be defined as places where $\nabla^2 z = 0$. We can apply the latter condition to the *Geomorphic Balance* to obtain an expression for the critical upslope area per contour width a_c at channel heads. We cannot eliminate all instances of the gradient in the *Hydromorphic Balance*, as it is present in the term $\cos(\theta) = \cos(\arctan|\nabla' z' h_g/\ell'_g|)$. Here we will make the assumption that the dimensionless gradient in this term is equal to one at channel heads, such that $\cos(\theta) \approx \cos(\arctan(\alpha))$.

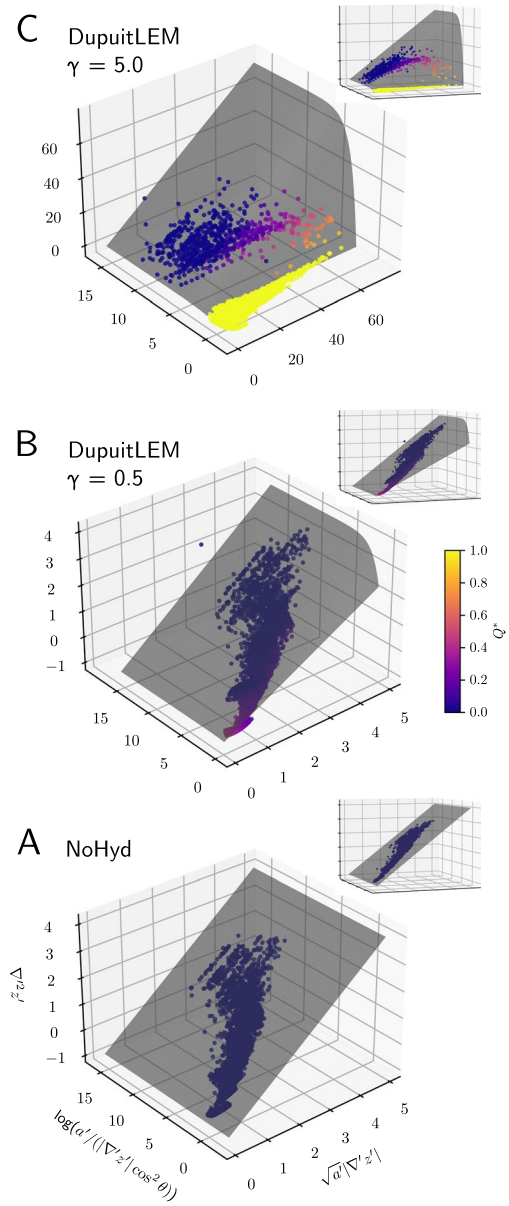

Figure 12. Plots of the manifold (gray) defined in Equation 59 and topography colored by Q^* showing how the form of the solution varies with γ. Both (b and c) have Hi = 5.0. The inset figures show the same results rotated 30° to emphasize how the solution compares to the steepness-curvature relationship.

If θ is similar at channel heads across our parameter space, this assumption should only affect the coefficient scaling γ and hillslope length. We must also choose a value for Q^* in order to find a solution for both the *Hydrologic balance* and *Geomorphic Balance*, as we have not eliminated it in this case. Our results show that Q^* can vary substantially at locations of zero Laplacian curvature (not shown), but here we will introduce a constant characteristic value Q_c^* for the purposes of finding a solution. Applying these conditions, we find that the *Hydromorphic Balance* gives an expression for the area per contour width at channel heads a_c:

$$\frac{a_c}{l_g} = \left(\frac{\gamma/Q_c^{*2}}{1+\alpha^2}\right)^{2/3} \tag{60}$$

$$= \left(\frac{bk_s}{pQ_c^{*2}}\frac{h_g}{h_g^2+l_g^2}\right)^{2/3} \tag{61}$$

or, expanding out the definitions of h_g and l_g, we can solve for the critical area at channel heads, $A_c = a_c v_0$:

$$A_c = \left(\frac{v_0 bk_s}{pQ_c^{*2}}\hat{h_g}\right)^{2/3} \tag{62}$$

where $\hat{h_g}$ is the inverse sum of two vertical length scales defined by the geomorphic variables:

$$\frac{1}{\hat{h_g}} = \frac{K}{U} + \frac{U}{\sqrt[3]{D^2 K v_0^2}} \tag{63}$$

The scaling confirms our previous observations that increasing the drainage capacity γ leads to greater spacing between channels, and therefore larger source areas at channel heads. Intuitively, this suggests that the landscape is less dissected when more flow drains through the subsurface. The expanded relationship shows a similar story: increasing $v_0 bk_s$ leads to larger contributing areas at channel heads, while increasing recharge rate p or effectiveness of fluvial incision relative to uplift lead to smaller contributing areas at channel heads. From here we further assume that the hillslope length at channel heads is proportional to the area per contour width, and thus $L_h/\ell_g \sim \gamma^{2/3}$. Despite the crudeness of this estimate, Figure 13 shows that this scaling is in agreement with the model results when $\gamma > 1$. Figure S7 in Supporting Information S1 shows that hillslope length does scale linearly with critical area per contour width. Additionally, Figure S8 in Supporting Information S1 shows an equivalent to Figure 13 which confirms the scaling with γ using an alternative metric that is very close to the definition of a_c used in the analysis here.

7. Discussion

7.1. Hydrogeomorphic Coevolution

The results presented here constitute one possible way that landscape history can be used to understand current hydrological processes by quantifying the coevolution of hydrological processes with landscape form (Harman & Troch, 2014; Troch et al., 2015). Prior research using coevolution to understand hydrological flow paths and processes focused on evolving subsurface properties. Jefferson et al. (2010) and Yoshida and Troch (2016) explore how flow paths evolve on constructional basaltic terrains, where porous young terrains tend to be highly permeable and drain flow vertically, while chemical weathering of basalt tends to progressively block flow paths with clays, leading to increased prevalence of lateral flow on older terrains. Both studies use space-for-time sub-

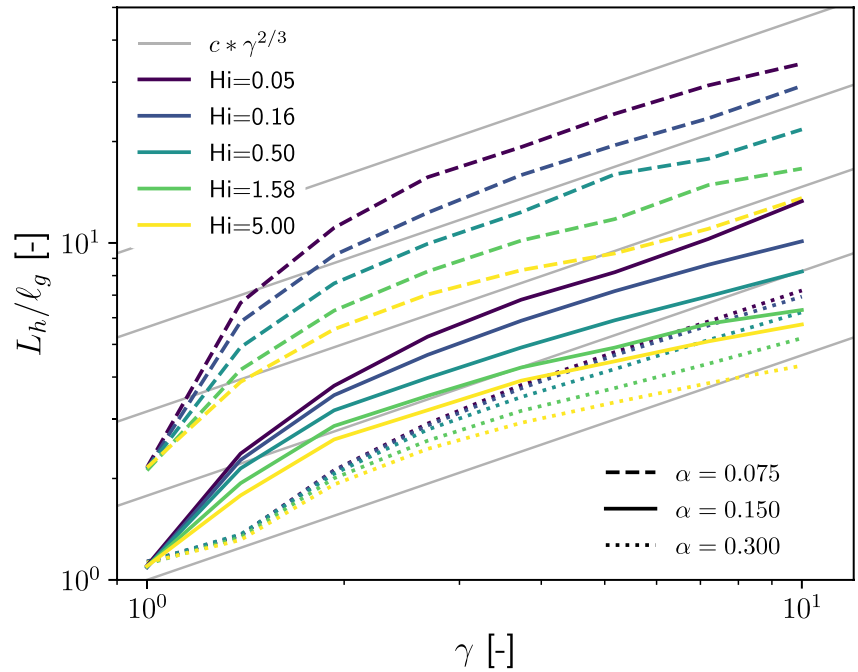

Figure 13. Hillslope length L_h increases with increasing γ. For a value of γ and α, L_h increases with decreasing Hi. Similarly, for a given value of γ and Hi, L_h increases with decreasing α. Gray lines with varying coefficients c show that the hillslope length scales approximately as $\gamma^{2/3}$ for $\gamma > 1$, which we derive from the *Hydromorphic Balance*.

stitution to explore temporal changes in drainage density, but find contradictory trends, suggesting that underlying processes of drainage and erosion are still not well enough understood in these landscapes. In contrast, recent work in denudational landscapes has focused on coevolution of subsurface flow paths and subsurface structure through the propagation of weathering fronts, in which porosity and permeability tend to increase as reactions take place and weathering products are removed (Brantley, Lebedeva, et al., 2017; Harman & Cosans, 2019; Harman & Kim, 2019). In these studies, continuous incision of streams is often used as a boundary condition to which hillslopes respond. In this study, we took a complementary approach, enforcing constant permeable thickness, hydraulic conductivity, and porosity, while exploring surface geomorphic evolution. We found that subsurface flow plays a critical role in setting hillslope length, which may in turn affect the hydraulic gradients and flow rates that affect subsurface weathering processes. Approaches focused on surface and subsurface may be unified to formulate more general theories of the evolution of denudational landscapes that could provide new insights or constraints on critical zone evolution hypotheses (Riebe et al., 2017).

7.2. Drainage Density, Lithology, and Transmissivity

One of the predictions of our model is a scaling relationship between subsurface drainage capacity and channel head contributing area per contour width, which should be comparable to a scaling relationship between transmissivity and hillslope length or drainage density. Linking drainage density to hydrological processes has long proven difficult. Early work on this topic by Carlston (1963) suggested an inverse relationship between drainage density and transmissivity, in agreement with what we observe in our numerical and analytical results. Carlston (1963) presented a negative correlation between drainage density and average baseflow for 13 humid climate watersheds as evidence of this relationship, though Dingman (1978) correctly argued that there is little physical basis to assume that mean baseflow scales with transmissivity. Challenges in estimating landscape scale transmissivity were clearly the limiting factor in this study, and they remain such today.

In other cases, factors not related to permeability may affect observed relationships. As mentioned previously, Jefferson et al. (2010) and Yoshida and Troch (2016) examined relationships between drainage density and age in basaltic landscapes, where permeability is expected to decrease and drainage density to increase with time. They found contradictory trends in drainage density with age, despite the fact that both studies found that

older, less permeable watersheds had the expected flashier, less subsurface-dominated runoff response. Other non-hydrological factors may be playing a larger role in controlling drainage density in certain sites. Recent studies using large sample sizes and high-resolution topography have examined relationships between drainage density and broad ranges of environmental controls, and have again come to disagreement. Sangireddy et al. (2016) concluded that lithology has no significant effect on drainage density among the 101 sites they examined. Meanwhile, Luo et al. (2016) examined drainage density across the contiguous United States and concluded that lithology is the dominant control in most regions other than coastal plains. While Luo et al. (2016) also examined hydraulic conductivity as a potential control on drainage density, finding it to be the dominant control in one small area in the interior of the United States, the data set used was itself derived from lithology and grain size data (Gleeson et al., 2014). Largely unknown covariation of many geomorphic and hydrologic properties with lithology is likely a source of uncertainty in the opposing trends observed in the previously mentioned studies. Consider, for example, how hydraulic conductivity of soils on a certain lithology covaries with hillslope transport rates, or bedrock erodibility. Untangling these covariations would be a useful research direction for continued understanding of landscape-hydrology coevolution.

Here we have examined the influence of subsurface hydrological conditions relative to climate (through γ and Hi) on topography in detail. The significance of this model is not that it accurately predicts the dynamics in a particular place, but that it captures the essence of a particular interaction between topography and subsurface properties via subsurface-driven runoff generation. With better data sets to help us understand the variation of subsurface properties in space, and covariation of hydrologic and geomorphic properties with lithology, we may use the information generated here to understand how the effects we have exposed here are manifested in real landscapes.

7.3. Scaling and Typology of Landscapes

Our similarity approach expands upon the analysis of Theodoratos et al. (2018) and Bonetti et al. (2020). The analysis conducted by Theodoratos et al. (2018) showed that by selecting appropriate length and time scales, a standard form of the streampower-linear diffusion LEM—which uses A rather than a and does not consider an incision threshold or runoff coefficient—was parameterless, and thus had only a single landscape typology—assessed on the basis of topography—that could be rescaled to obtain every result the model could produce. As pointed out by Bonetti et al. (2020), the streampower-linear diffusion LEM does have an additional parameter, which is unaccounted for in Theodoratos et al. (2018) because the authors do not expose the differential equation that defines the upslope area per contour width. With this equation expressed, Bonetti et al. (2020) develop a nondimensionalization where one parameter remains, similar to the Peclet number that appears in Perron et al. (2008). Our analysis of the streampower-linear diffusion LEM (called the *NoHyd* model here) shows that a parameterless set of equations can still be obtained from the governing equations when accounting for the upslope area differential equation. We show that, contrary to Bonetti et al. (2020), there is a single typology for the *NoHyd* model, which can be rescaled to obtain all results the model may produce.

We develop the scaling analysis further by including the effects of runoff generated from shallow unconfined groundwater flow. This introduces four dimensionless parameters, of which three are important for the emergent topography. With this model, there is no longer a single landscape typology, but variation in form dependent on how flow is partitioned between surface and subsurface γ, the degree to which topography drives groundwater flow Hi, and the landscape gradient generated by underlying geomorphic processes α.

Other typologies are certainly obtainable through the addition of other geomorphic or hydrologic processes, including a fluvial incision threshold (Theodoratos & Kirchner, 2020a). While at first it may appear that our runoff generation factor Q^* should have a similar effect—and consequently produce a similar typology—to a fluvial incision threshold, this is not the case, as their dependence on topographic slope is opposite. A given threshold for surface water erosion is more likely to be exceeded when topographic gradient is steeper, because the flow will tend to exert a higher tractive stress on the surface. However, surface water flow should be less likely to occur on steeper slopes, as hydraulic gradients in shallow aquifers will increase, increasing subsurface flow capacity. Consequently, fluvial incision threshold and runoff generation thresholds should produce different characteristic typologies in topography. The model we present here is unique in that it expresses feedbacks between hydrologic and geomorphic processes, which consequently link landscape typology to hydrologic function. While we have limited our consideration in this study to only the most basic of geomorphic processes, the scaling framework presented here could be readily expanded to include other processes should they be necessary to capture a particular environment or hydrogeomorphic feedback.

7.4. Characteristic Contour Width and Valley Transmissivity

We first introduced the concept of a characteristic contour width v_0 in order to write the channel scaling relationship (Equation 7) in terms of upslope area per contour width a rather than upslope area A. This proved useful in subsequent scaling analyses, where we developed a new parameterless scaling of the governing geomorphic equations that is only possible because we have accounted for v_0 in our definitions of the geomorphic length, height, and timescales ℓ_g^*, h_g, and t_g. We noted previously there that we are free to choose a value of v_0, as there will always be a corresponding value of k_w to satisfy the relationship between w and a. What then is a physically meaningful characteristic contour width, and how would we identify it outside of the context of a landscape evolution model? One possible explanation appears in the hydromorphic balance Equation 62 for the upslope area at channel heads, A_c. Here the characteristic contour width appears in the numerator $v_0 b k_s$, which is effectively the transmissivity integrated across a characteristic contour width. This integrated transmissivity is particularly important at channel heads, where relative magnitudes of surface and subsurface flow are similar. Upstream of the channel head, the contour width is less important, as topographic features do not constrict groundwater flow to a fixed width. Further downstream from the channel head, groundwater flow is constricted by the valley width, but most of the discharge will be transmitted as surface water rather than groundwater. Because A_c scales with v_0 just as it does with the transmissivity bk_s, v_0 plays a critical role in determining the extent of landscape dissection, as increasing channel head source areas increases the distance from channels to ridges. In landscapes similar to those modeled here, we suggest that the characteristic contour width is best thought of as characteristic channel head width, and that more attention should be paid to this factor in field investigations.

7.5. Landscape Complexity

In developing this first systematic exploration of the effects of subsurface flow on steady-state landscape form, we have neglected the complexity of landscape processes and heterogeneity of landscape properties in favor of an approach with a tractable number of parameters so that we can explore the diversity of behaviors it can produce. However, it is likely that processes and heterogeneity not captured here have significant impacts on landscape form. Subsurface properties are not only heterogeneous, but spatially organized, including systematic variations in permeability with depth through soil and weathered bedrock and along hillslope catenas (Lohse & Dietrich, 2005). The scope of runoff generation processes we have examined is also limited, as we have not considered infiltration excess overland flow, nor other erosional processes that are linked to shallow groundwater, including seepage erosion (Abrams et al., 2009; Laity & Malin, 1985) and landsliding driven by excess pore water pressure (Montgomery & Dietrich, 1994). Likewise, ecological processes may act on the environment in ways that cannot be captured by the processes and parameters included here. For example, feedback between depth to water table and tree growth may affect spatial patterns of hillslope and fluvial sediment transport, as trees anchor sediment with roots, displace sediment through treethrow, or encourage soil production (Brantley, Eissenstat, et al., 2017; Gabet & Mudd, 2010).

7.6. Steady-State Topography

In this study we have focused on evaluating landscapes near topographic steady state in order to understand the emergent relationships between topography and hydrology generated by these governing equations. This is a powerful method employed in landscape evolution modeling studies to understand the form toward which landscapes will evolve (e.g., Perron et al., 2008; Theodoratos et al., 2018). In the model we have used here, however, times to steady state are long (millions to tens of millions of years) compared to real timescales of variability in climate and baselevel change. For this reason, transience, at least in some portions of the landscape, is likely the norm in real landscapes with similar dominant processes to those modeled here (Whipple, 2001). On the other hand, nonlinear models of hillslope diffusion show substantially shorter times to steady state (Roering et al., 2001), which may be important when hillslopes are the limiting factor in reaching topographic steady state. Further investigation could focus on transient responses the model considered here, which may provide insights into a wider range of humid landscapes.

7.7. Steady Recharge

In this model, we have shown that runoff generation from shallow groundwater driven by steady recharge has a strong effect on emergent landscape properties. With increasing γ, we found that the hydrological function of

the landscape was increasingly binary: channels have surface runoff nearly equal to the recharge rate integrated over the area upslope, while hillslopes do not contribute surface runoff at all. While this may be characteristic of some landscapes where saturated areas are more or less constant in time, in many places, saturated areas and wetted channels expand and contract in response to the arrival of storm events or snow melt (Antonelli et al., 2020; Dunne & Black, 1970; Nippgen et al., 2015). Furthermore, antecedent wetness plays an important role in determining the hydrological response to precipitation (Longobardi et al., 2003; O'Loughlin, 1981). As fluvial sediment transport in our model is proportional to runoff Q^*, we expect that precipitation variability and subsurface water storage would affect sediment transport, ultimately affecting the landscape form as well. Previous studies have shown that landscape form and channel profiles have are sensitive to variability in precipitation or discharge, depending on factors including the presence of erosion thresholds and the nonlinearity of the fluvial incision model (Deal et al., 2018; Lague et al., 2005; Tucker, 2004). In a future contribution, we will extend the theoretical framework used here to incorporate stochastic precipitation, allowing us to explore the emergence of hydrogeomorphic features such as runoff variable source areas.

8. Conclusion

Here we have coupled a model of shallow groundwater flow with a model of denudational landscape evolution, and have shown the first results of such a model at topographic steady state. The shallow aquifer model uses the Dupuit-Forcheimer assumptions to generate lateral groundwater flow and surface water discharge from groundwater return flow and precipitation on saturated areas. The topography evolves due to fluvial incision by runoff generated by the groundwater model, linear hillslope diffusion, and a constant rate of uplift. We use a novel scaling analysis to guide our numerical simulations, and find that the subsurface drainage capacity relative to climate plays a critical role in setting topographic properties including hillslope length. We showed that the linear relationship between steepness and Laplacian curvature that emerges from the simple streampower incision-linear diffusion LEM bifurcates with increasing subsurface drainage capacity: saturated areas tend toward the linear relationship between steepness and curvature, while unsaturated hillslopes maintain constant negative curvature regardless of steepness. By combinging the steady-state solutions of the hydrological and geomorphic models, we find that all locations contributing runoff lie near a manifold that relates steepness, Laplacian curvature, and topographic index. This contrasts with the simpler linear relationship between steepness and Laplacian curvature that is found in the absence of runoff generation from the shallow subsurface. A complementary analysis of the governing equations at steady state showed that hillslope length should scale with the subsurface drainage capacity, and therefore the transmissivity, to the power 2/3. This was supported by our numerical results for sufficiently large subsurface drainage capacities. Links between landscape form and hydrologic function have been long sought-after in hydrology. By analyzing these interactions in an idealized model framework, we have demonstrated the potential for subsurface hydrologic properties to profoundly influence surface morphology. However, it remains extremely challenging to test whether the predictions of this model are (in detail) representative of real landscapes.

Appendix A: DupuitLEM Dimensionless Equations From Symmetry Groups

Here we extend the scaling analysis applied to the *NoHyd* model to include the governing hydrological equations in *DupuitLEM*. Because the hydrological model is linked to the geomorphic model through Q^*, the set of transformations used for the geomorphic equations above is not necessarily applicable to *DupuitLEM*. In addition to the characteristic scales ℓ_g, h_g, and t_g used for the *NoHyd* model, we will introduce two scales particularly relevant to hydrological processes: a characteristic aquifer thickness h_a and a characteristic aquifer drainage time t_d. First we derive these quantities. A simple steady-state mass balance of water in a 1D hillslope with length ℓ_g, relief h_g, recharge rate p, and hydraulic conductivity k_s gives:

$$p\ell_g = h_a k_s h_g / \ell_g. \tag{A1}$$

assuming all flow leaves downslope through the subsurface. It is worth noting that because topography and hydrology evolve together in our model, we do not know what the actual mean hillslope length and relief will be. Nonetheless, incorporating h_g and ℓ_g as characteristic hillslope scales allows us to capture some dependence of emergent topographic properties on underlying geomorphic processes. The characteristic drainage time for a

shallow aquifer can be derived from Harman and Sivapalan (2009, their Equation 6), which likewise describes the drainage of an aquifer with characteristic length and relief with drainable porosity n_e:

$$t_d = \frac{\ell_g n_e}{k_s \sin\theta} \tag{A2}$$

Making the approximation $\sin(\theta) \sim h_g/\ell_g$, the resulting characteristic scales are:

$$h_a = \frac{p\ell_g}{k_s h_g/\ell_g} \tag{A3}$$

$$t_d = \frac{\ell_g n_e}{k_s h_g/\ell_g} \tag{A4}$$

In addition to the recast landscape evolution model in Equations 20 and 21, we add those of the hydrological model, replacing parameters with equivalent combinations of the characteristic scales:

$$\frac{\partial h}{\partial t} = \frac{h_a}{t_d}\left(1 - \frac{\nabla \cdot q}{p} - \frac{q_s}{p}\right) \tag{A5}$$

$$\frac{q}{p} = -h\cos^2(\arctan|\nabla z|)\frac{\ell_g^2}{h_g h_a}(\nabla h + \nabla z) \tag{A6}$$

$$\frac{q_s}{p} = \mathcal{G}\left(\frac{h}{b}\right)\mathcal{R}\left(1 - \frac{\nabla \cdot q}{p}\right) \tag{A7}$$

$$Q^* = \frac{1}{Ap}\int_A q_s \, dA_c \tag{A8}$$

Here we have expanded the aquifer base angle $\theta = \arctan|\nabla z_b| = \arctan|\nabla z|$, as constant permeable thickness implies that the aquifer base gradient is equal to the topographic gradient. As with the scaling analysis in Equations 20 and 21, we can look for sets of transformations under which the equations are invariant. The symmetry group for the time dimension shown in Equation 28 will apply as before. However we cannot separately transform the vertical and horizontal length scales in the hydrologic equations. This is because we cannot cancel a scaling factor on ∇ in the cosine term of Equation A6 without scaling z as well, and vice versa. As a result, horizontal and vertical dimensions must be transformed together, leaving only two symmetry groups that produce invariance:

$$\begin{aligned}&\{t \to ct,\ \ t_g \to ct_g,\ \ t_d \to ct_d\}\\ &\{x \to cx,\ \ y \to cy,\ \ a \to ca,\ \ A \to c^2A,\ \ l_g \to cl_g,\\ &\quad q \to cq,\ \ z \to cz,\ \ h \to ch,\ \ h_g \to ch_g,\ \ h_a \to ch_a,\ \ b \to cb\}\end{aligned} \tag{A9}$$

Again, we can choose particular values for scaling factors c and apply the transformations in the symmetry groups in search of a form that eliminates or consolidates the characteristic scales. We will first apply the time symmetry group, choosing $c = 1/(t_g t_d)$. This is equivalent to applying the transformations in the group twice, once with $c = 1/t_g$ and again with $c = 1/t_d$. We will then apply the second group, choosing $c = 1/(\ell_g h_g h_a)$. Likewise, this is equivalent to applying it three times with each of the three factors in the denominator. Applying these scales, we obtain the dimensionless form of the hydrological equations, presented in the main text (Equations 35–40).

Appendix B: Scaling Analysis in Special Cases

The governing hydrological equations account for the effects of gradients in aquifer thickness and gradients in aquifer base elevation in driving groundwater flow. These equations can be simplified under conditions where one gradient is more important than the other, reducing the constraints on our symmetry groups. Suppose that topographic gradients are generally insignificant, and groundwater flow is driven by gradients in aquifer thickness ($\nabla h \gg \nabla z$). In this case, the expression for groundwater specific-discharge changes, as we can approximate

$\cos\theta \approx 1$ and $\nabla z \approx 0$ for the purposes of groundwater flow. Then the governing equations are the same except for q:

$$\frac{q}{p} = -h\frac{\ell_g^2}{h_g h_a}\nabla h \tag{B1}$$

In this case, because the cosine term does not appear, ℓ_g and h_g need not be scaled together, as discussed in Appendix A. There are now three transformations that maintain symmetry. Namely we no longer need to scale horizontal and vertical dimensions together, but we do need scale to aquifer thickness h with the vertical scales in order to maintain consistency in the groundwater specific-discharge equation.

$$\begin{gathered}\{t \to ct,\ \ t_g \to ct_g,\ \ t_d \to ct_d\} \\ \{h \to ch,\ \ h_a \to ch_a,\ \ b \to cb,\ \ z \to cz,\ \ h_g \to ch_g\} \\ \left\{x \to cx,\ \ y \to cy,\ \ a \to ca,\ \ A \to c^2 A,\ \ l_g \to cl_g,\ \ q \to cq\right\}\end{gathered} \tag{B2}$$

Noting the similarities with the transformation of the full *DupuitLEM* equations, we select the scales $c = 1/(t_g t_d)$, $c = 1/(h_a h_g)$, and $c = 1/\ell_g$ respectively. We arrive at a rescaled set of governing equations for the case in which flow is primarily driven by gradients in aquifer thickness. The result is the same as Equations 35–40, except that the equation for q' (Equation 38) has changed to

$$q' = -h'\frac{\nabla' h'}{\mathrm{Hi}}. \tag{B3}$$

Under these conditions, the hillslope number $\mathrm{Hi} = h_g/h_a$ still appears in the groundwater specific-discharge expression, while the characteristic gradient $\alpha = h_g/\ell_g$ no longer appears. This suggests that as Hi becomes small, the sensitivity to Hi does not decrease, but sensitivity to α does decrease. Small Hi indicates that water-table gradients are more important than topographic gradients in driving flow. As α is an indicator of topographic gradients, it is appropriate that it should diminish in importance when Hi is small.

Conversely, suppose that relief is generally large in comparison to aquifer thickness, $h_g \gg h_a$, in which case the hillslope number $\mathrm{Hi} \gg 1$. Consequently, topographic gradients rather than aquifer thickness gradients tend to drive groundwater flow. In this case we neglect ∇h, altering the groundwater specific-discharge expression (Equation A6) to

$$\frac{q}{p} = -h\cos^2(\arctan|\nabla z|)\frac{\ell_g^2}{h_g h_a}\nabla z. \tag{B4}$$

Applying our symmetry method as before, we find that ℓ_g and h_g must still be scaled together. However, this time, aquifer thickness h need not be scaled with these simultaneously in order to obtain a consistent set of equations. Instead, there are now three sets of transformations that comprise the symmetry:

$$\begin{gathered}\{t \to ct,\ \ t_g \to ct_g,\ \ t_d \to ct_d\} \\ \{h \to ch,\ \ h_a \to ch_a,\ \ b \to cb\} \\ \left\{x \to cx,\ \ y \to cy,\ \ a \to ca,\ \ A \to c^2 A,\ \ l_g \to cl_g,\right. \\ \left.\quad q \to cq,\ \ \ z \to cz,\ \ h_g \to ch_g\right\}\end{gathered} \tag{B5}$$

Implementing the three transformations above with $c = 1/(t_g t_d)$, $c = 1/h_a$, and $c = 1/(h_g \ell_g)$ respectively, we arrive at a rescaled set of governing equations that are the same as those found in Equations 35–40, only again with an altered expression for q':

$$q' = -h'\cos^2(\arctan|\nabla' z' h_g/\ell_g|)\nabla' z' \tag{B6}$$

Here the hillslope number Hi no longer appears in the equation. This suggests that the solution to the full governing equations should be independent of Hi when Hi is large. This makes sense in the context of Equation 38, as 1/Hi multiplies the gradient in aquifer thickness, which should be small relative to topographic gradients when Hi is large.

Notation

Variable definitions are below, with dimensions length L, time T, and mass M. Prime always indicates the dimensionless equivalent, where dimensionless equivalents are defined in the text.

Variable	Name	Dimension
x, y	Horizontal coordinates	L
T	Time	T
$z(x, y)$	Topographic elevation	L
$h(x, y)$	Aquifer thickness	L
$A(x, y)$	Area upslope	L^2
$a(x, y)$	Area upslope per unit contour width	L
$\theta(x, y)$	Aquifer base slope angle	rad
h_g	Characteristic geomorphic height scale	L
ℓ_g	Characteristic geomorphic length scale	L
t_g	Characteristic geomorphic time scale	T
h_a	Characteristic aquifer thickness	L
t_d	Characteristic time to drain aquifer storage	T
δ	Timescale factor	–
α	Characteristic gradient	–
γ	Drainage capacity	–
Hi	Hillslope number	–
E_f	Fluvial incision rate	L/T
E_h	Hillslope diffusion rate	L/T
U	Uplift rate	L/T
K	Streampower incision coefficient	$1/T$
m	Streampower area exponent	–
n	Streampower slope exponent	–
v_0	Characteristic contour width	L
τ	Bed shear stress	M/LT^2
τ_c	Critical bed shear stress	M/LT^2
k_e	Erosivity coefficient	$M^{-\beta}L^{1+\beta}T^{2\beta-1}$
β	Shear stress exponent	–
ρ_w	Density of water	M/L^3
g	Acceleration due to gravity	L/T^2
d_f	Channel flow depth	L
C	Chezy coefficient	$L^{1/2}/T$
w	Channel width	L

Variable	Name	Dimension
k_w	Width coefficient	–
b	Permeable thickness	L
q_h	Hillslope sediment transport rate	L^2/T
D	Hillslope diffusivity	L^2/T
k_{sf}	Timestep scaling factor	–
$q(x, y, t)$	Groundwater specific-discharge	L^2/T
$q_s(x, y, t)$	Local surface runoff	L/T
$Q(x, y, t)$	Discharge	L^3/T
$Q^*(x, y, t)$	Dimensionless discharge	–
p	Recharge rate	L/T
k_s	Hydraulic conductivity	L/T
n_e	Drainable porosity	–
$\mathcal{G}$	Step function	
$\mathcal{R}$	Ramp function	
a_c	Critical area per contour width	L
A_c	Critical area	L^2
L_h	Mean hillslope length	L

Data Availability Statement

No original data is presented in this paper. Model output has been archived at doi.org/10.5281/zenodo.5523187. The Python package DupuitLEM v1.0 (Litwin et al., 2021) contains the models and scripts used to generate output, post-process output, and create figures presented here. Landlab v2.0 (Hutton et al., 2020) is a core dependency of DupuitLEM, while NumPy (Harris et al., 2020), Pandas (Pandas Development Team, 2020), and Matplotlib (Hunter, 2007) were used for additional analysis and visualization. The complete list of input parameter values can be found in Table S1 of Supporting Information S1. Simulations were carried out at the Maryland Advanced Research Computing Center (marcc.jhu.edu) funded by the state of Maryland.

Acknowledgments
This work was supported by NSF grants EAR-2012264, EAR-1654194, ACI-1450409, EAR-1725774, and EAR-1831623. The authors would like to thank Clément Roques and two anonymous reviewers for their comments which have significantly improved the manuscript.

References

Abrams, D. M., Lobkovsky, A. E., Petroff, A. P., Straub, K. M., McElroy, B., Mohrig, D. C., et al. (2009). Growth laws for channel networks incised by groundwater flow. *Nature Geoscience*, *2*(3), 193–196. https://doi.org/10.1038/ngeo432

Ahnert, F. (1976). Brief description of a comprehensive three-dimensional process-response model of landform development. *Zeitschrift für Geomorphologie, Supplementbände*, *25*, 29–49.

Antonelli, M., Glaser, B., Teuling, A. J., Klaus, J., & Pfister, L. (2020). Saturated areas through the lens: 1. Spatio-temporal variability of surface saturation documented through thermal infrared imagery. *Hydrological Processes*, *34*(6), 1310–1332. https://doi.org/10.1002/hyp.13698

Armstrong, A. (1976). A three-dimensional simulation of slope forms. *Zeitschrift für Geomorphologie, Supplementbände*, *25*, 20–28.

Barenblatt, G. I. (1996). *Scaling, self-similarity, and intermediate asymptotics* (Vol. 14). Cambridge University Press.

Barnhart, K. R., Hutton, E. W. H., Tucker, G. E., Gasparini, N. M., Istanbulluoglu, E., Hobley, D. E. J., et al. (2020). Short communication: Landlab v2.0: A software package for Earth surface dynamics. *Earth Surface Dynamics*, *8*(2), 379–397. https://doi.org/10.5194/esurf-8-379-2020

Barnhart, K. R., Tucker, G. E., Doty, S. G., Glade, R. C., Shobe, C. M., Rossi, M. W., & Hill, M. C. (2020). Projections of landscape evolution on a 10,000 year timescale with assessment and partitioning of uncertainty sources. *Journal of Geophysical Research: Earth Surface*, *125*(12), e2020JF005795. https://doi.org/10.1029/2020JF005795

Barnhart, K. R., Tucker, G. E., Doty, S. G., Shobe, C. M., Glade, R. C., Rossi, M. W., & Hill, M. C. (2020). Inverting topography for landscape evolution model process representation: 3. Determining parameter ranges for select mature geomorphic transport laws and connecting changes in fluvial erodibility to changes in climate. *Journal of Geophysical Research: Earth Surface*, *125*(7), e2019JF005287. https://doi.org/10.1029/2019JF005287

Berne, A., Uijlenhoet, R., & Troch, P. A. (2005). Similarity analysis of subsurface flow response of hillslopes with complex geometry. *Water Resources Research*, *41*(9), 1–10. https://doi.org/10.1029/2004WR003629

Beven, K. J., & Kirkby, M. J. (1979). A physically based, variable contributing area model of basin hydrology. *Hydrological Sciences Bulletin*, *24*(1), 43–69. https://doi.org/10.1080/02626667909491834

Bishop, P. (2007). Long-term landscape evolution: Linking tectonics and surface processes. *Earth Surface Processes and Landforms*, *32*(3), 329–365. https://doi.org/10.1002/esp.1493

Bonetti, S., Bragg, A. D., & Porporato, A. (2018). On the theory of drainage area for regular and non-regular points. *Proceedings of the Royal Society A: Mathematical, Physical and Engineering Sciences*, *474*(2211), 20170693. https://doi.org/10.1098/rspa.2017.0693

Bonetti, S., Hooshyar, M., Camporeale, C., & Porporato, A. (2020). Channelization cascade in landscape evolution. *Proceedings of the National Academy of Sciences*, *117*(3), 1375–1382. https://doi.org/10.1073/pnas.1911817117

Brantley, S. L., Eissenstat, D. M., Marshall, J. A., Godsey, S. E., Balogh-Brunstad, Z., Karwan, D. L., et al. (2017). Reviews and syntheses: On the roles trees play in building and plumbing the critical zone. *Biogeosciences*, *14*(22), 5115–5142. https://doi.org/10.5194/bg-14-5115-2017

Brantley, S. L., Lebedeva, M. I., Balashov, V. N., Singha, K., Sullivan, P. L., & Stinchcomb, G. (2017). Toward a conceptual model relating chemical reaction fronts to water flow paths in hills. *Geomorphology*, *277*, 100–117. https://doi.org/10.1016/j.geomorph.2016.09.027

Braun, J., & Willett, S. D. (2013). A very efficient O(n), implicit and parallel method to solve the stream power equation governing fluvial incision and landscape evolution. *Geomorphology*, *180–181*, 170–179. https://doi.org/10.1016/j.geomorph.2012.10.008

Bresciani, E., Davy, P., & de Dreuzy, J.-R. (2014). Is the Dupuit assumption suitable for predicting the groundwater seepage area in hillslopes? *Water Resources Research*, *50*(3), 2394–2406. https://doi.org/10.1002/2013WR014284

Brocca, L., Melone, F., Moramarco, T., & Singh, V. P. (2009). Assimilation of observed soil moisture data in storm rainfall-runoff modeling. *Journal of Hydrologic Engineering*, *14*(2), 153–165. https://doi.org/10.1061/(ASCE)1084-0699(2009)14:2(153)

Brutsaert, W. (2005). *Hydrology: An introduction*. Cambridge University Press. Retrieved from https://books.google.com/books?id=yX_xS55xxyoC

Carlston, C. W. (1963). *Drainage density and streamflow*. U.S. Government Printing Office.

Chen, A., Darbon, J., & Morel, J.-M. (2014). Landscape evolution models: A review of their fundamental equations. *Geomorphology*, *219*, 68–86. https://doi.org/10.1016/j.geomorph.2014.04.037

Childs, E. C. (1971). Drainage of groundwater resting on a sloping bed. *Water Resources Research*, *7*(5), 1256–1263. https://doi.org/10.1029/WR007i005p01256

Deal, E., Braun, J., & Botter, G. (2018). Understanding the role of rainfall and hydrology in determining fluvial erosion efficiency. *Journal of Geophysical Research: Earth Surface*, *123*(4), 744–778. https://doi.org/10.1002/2017JF004393

Dietrich, W. E., Bellugi, D. G., Sklar, L. S., Stock, J. D., Heimsath, A. M., & Roering, J. J. (2003). Geomorphic transport laws for predicting landscape form and dynamics. In P. R. Wilcock & R. M. Iverson (Eds.), *Geophysical Monograph Series* (pp. 103–132). American Geophysical Union. Retrieved from http://doi.wiley.com/10.1029/135GM09

Dietrich, W. E., Wilson, C. J., Montgomery, D. R., & McKean, J. (1993). Analysis of erosion thresholds, channel networks, and landscape morphology using a digital terrain model. *The Journal of Geology*, *101*(2), 259–278. https://doi.org/10.1086/648220

Dingman, S. L. (1978). Drainage density and streamflow: A closer look. *Water Resources Research*, *14*(6), 1183–1187. https://doi.org/10.1029/WR014i006p01183

Dunne, T. (1978). Field studies of hillslope flow processes. In M. J. Kirkby (Ed.), *Hillslope hydrology*. Wiley.

Dunne, T., & Black, R. D. (1970). Partial area contributions to storm runoff in a small New England watershed. *Water Resources Research*, *6*(5), 1296–1311. https://doi.org/10.1029/WR006i005p01296

Forte, A. M., Yanites, B. J., & Whipple, K. X. (2016). Complexities of landscape evolution during incision through layered stratigraphy with contrasts in rock strength. *Earth Surface Processes and Landforms*, *41*(12), 1736–1757. https://doi.org/10.1002/esp.3947

Gabet, E. J., & Mudd, S. M. (2009). A theoretical model coupling chemical weathering rates with denudation rates. *Geology*, *37*(2), 151–154. https://doi.org/10.1130/G25270A.1

Gabet, E. J., & Mudd, S. M. (2010). Bedrock erosion by root fracture and tree throw: A coupled biogeomorphic model to explore the humped soil production function and the persistence of hillslope soils. *Journal of Geophysical Research: Earth Surface*, *115*(F4). https://doi.org/10.1029/2009JF001526

Gleeson, T., Moosdorf, N., Hartmann, J., & van Beek, L. P. H. (2014). A glimpse beneath earth's surface: GLobal HYdrogeology MaPS (GLHYMPS) of permeability and porosity. *Geophysical Research Letters*, *41*(11), 3891–3898. https://doi.org/10.1002/2014GL059856

Harman, C. J., & Cosans, C. L. (2019). A low-dimensional model of bedrock weathering and lateral flow coevolution in hillslopes: 2. Controls on weathering and permeability profiles, drainage hydraulics, and solute export pathways. *Hydrological Processes*, *33*(8), 1168–1190. https://doi.org/10.1002/hyp.13385

Harman, C. J., & Kim, M. (2019). A low-dimensional model of bedrock weathering and lateral flow coevolution in hillslopes: 1. Hydraulic theory of reactive transport. *Hydrological Processes*, *33*(4), 466–475. https://doi.org/10.1002/hyp.13360

Harman, C. J., & Sivapalan, M. (2009). A similarity framework to assess controls on shallow subsurface flow dynamics in hillslopes. *Water Resources Research*, *45*(1), 1–12. https://doi.org/10.1029/2008WR007067

Harman, C. J., & Troch, P. A. (2014). What makes Darwinian hydrology "Darwinian"? Asking a different kind of question about landscapes. *Hydrology and Earth System Sciences*, *18*(2), 417–433. https://doi.org/10.5194/hess-18-417-2014

Harris, C. R., Millman, K. J., van der Walt, S. J., Gommers, R., Virtanen, P., Cournapeau, D., et al. (2020). Array programming with NumPy. *Nature*, *585*(7825), 357–362. https://doi.org/10.1038/s41586-020-2649-2

Hewlett, J. D., & Hibbert, A. R. (1967). Factors affecting the response of small watersheds to precipitation in humid areas. *Int. Symp. Forest Hydrology*, *33*, 288–293. https://doi.org/10.1177/0309133309338118

Hobley, D. E. J., Adams, J. M., Nudurupati, S. S., Hutton, E. W. H., Gasparini, N. M., Istanbulluoglu, E., & Tucker, G. E. (2017). Creative computing with Landlab: An open-source toolkit for building, coupling, and exploring two-dimensional numerical models of earth-surface dynamics. *Earth Surface Dynamics*, *5*(1), 21–46. https://doi.org/10.5194/esurf-5-21-2017

Horton, R. E. (1945). Erosional development of streams and their drainage basins; hydrophysical approach to quantitative morphology. *Geological Society of America Bulletin*, *56*(3), 275–370. https://doi.org/10.1130/0016-7606(1945)56[275:EDOSAT]2.0.CO;2

Howard, A. D. (1994). A detachment-limited model of drainage basin evolution. *Water Resources Research*, *30*(7), 2261–2285. https://doi.org/10.1029/94WR00757

Howard, A. D., & Kerby, G. (1983). Channel changes in badlands. *Geological Society of America Bulletin*, *94*(6), 739–752. https://doi.org/10.1130/0016-7606(1983)94<739:ccib>2.0.co;2

Huang, X., & Niemann, J. D. (2006). Modelling the potential impacts of groundwater hydrology on long-term drainage basin evolution. *Earth Surface Processes and Landforms*, *31*, 1802–1823. https://doi.org/10.1002/esp.1369

Huang, X., & Niemann, J. D. (2008). How do streamflow generation mechanisms affect watershed hypsometry? *Earth Surface Processes and Landforms*, *33*, 751–772. https://doi.org/10.1002/esp.1573

Hunter, J. D. (2007). Matplotlib: A 2D graphics environment. *Computing in Science & Engineering*, *9*(3), 90–95. https://doi.org/10.1109/MCSE.2007.55

Hutton, E., Barnhart, K., Hobley, D., Tucker, G., Nudurupati, S. S., Adams, J., et al. (2020). *landlab/landlab. Mrs. Weasley*. Zenodo. https://doi.org/10.5281/zenodo.3776837

Ijjász-Vásquez, E. J., Bras, R. L., & Moglen, G. E. (1992). Sensitivity of a basin evolution model to the nature of runoff production and to initial conditions. *Water Resources Research*, *28*(10), 2733–2741. https://doi.org/10.1029/92WR01561

Jefferson, A., Grant, G. E., Lewis, S. L., & Lancaster, S. T. (2010). Coevolution of hydrology and topography on a basalt landscape in the Oregon Cascade Range, USA. *Earth Surface Processes and Landforms*, *35*(7), 803–n. https://doi.org/10.1002/esp.1976

Lague, D., Hovius, N., & Davy, P. (2005). Discharge, discharge variability, and the bedrock channel profile. *Journal of Geophysical Research: Earth Surface*, *110*(F4). https://doi.org/10.1029/2004JF000259

Laity, J. E., & Malin, M. C. (1985). Sapping processes and the development of theater-headed valley networks on the Colorado Plateau. *Geological Society of America Bulletin*, *96*, 203–217. https://doi.org/10.1130/0016-7606(1985)96<203:spatdo>2.0.co;2

Lapides, D. A., David, C., Sytsma, A., Dralle, D., & Thompson, S. (2020). Analytical solutions to runoff on hillslopes with curvature: Numerical and laboratory verification. *Hydrological Processes*, *34*(24), 4640–4659. https://doi.org/10.1002/hyp.13879

Leopold, L. B., & Maddock, T. (1953). *The hydraulic geometry of stream channels and some physiographic implications*. U.S. Government Printing Office.

Litwin, D. G., Barnhart, K. R., Tucker, G. E., & Harman, C. J. (2021). *DupuitLEM: groundwater landscape evolution with Landlab*. Zenodo. https://doi.org/10.5281/zenodo.5522828

Litwin, D. G., Tucker, G., Barnhart, K., & Harman, C. J. (2020). GroundwaterDupuitPercolator: A Landlab component for groundwater flow. *Journal of Open Source Software*, *5*(46), 1935. https://doi.org/10.21105/joss.01935

Lohse, K. A., & Dietrich, W. E. (2005). Contrasting effects of soil development on hydrological properties and flow paths. *Water Resources Research*, *41*(12), 1–17. https://doi.org/10.1029/2004WR003403

Longobardi, A., Villani, P., Grayson, R. B., & Western, A. W. (2003). On the relationship between runoff coefficient and catchment initial conditions. *Modelling and Simulation Society of Australia and New Zealand*, *2*(1), 1–6.

Luo, W., Jasiewicz, J., Stepinski, T., Wang, J., Xu, C., & Cang, X. (2016). Spatial association between dissection density and environmental factors over the entire conterminous United States. *Geophysical Research Letters*, *43*(2), 692–700. https://doi.org/10.1002/2015GL066941

Manga, M. (1996). Hydrology of spring-dominated streams in the Oregon Cascades. *Water Resources Research*, *32*(8), 2435–2439. https://doi.org/10.1029/96WR01238

Marçais, J., de Dreuzy, J. R., & Erhel, J. (2017). Dynamic coupling of subsurface and seepage flows solved within a regularized partition formulation. *Advances in Water Resources*, *109*, 94–105. https://doi.org/10.1016/j.advwatres.2017.09.008

Martin, Y., & Church, M. (2004). Numerical modelling of landscape evolution: Geomorphological perspectives. *Progress in Physical Geography: Earth and Environment*, *28*(3), 317–339. https://doi.org/10.1191/0309133304pp412ra

Montgomery, D. R., & Dietrich, W. E. (1994). A physically based model for the topographic control on shallow landsliding. *Water Resources Research*, *30*(4), 1153–1171. https://doi.org/10.1029/93WR02979

Nippgen, F., McGlynn, B. L., & Emanuel, R. E. (2015). The spatial and temporal evolution of contributing areas. *Water Resources Research*. https://doi.org/10.1002/2014WR016719

O'Loughlin, E. M. (1981). Saturation regions in catchments and their relations to soil and topographic properties. *Journal of Hydrology*, *53*(3–4), 229–246. https://doi.org/10.1016/0022-1694(81)90003-2

Pandas Development Team. (2020). *pandas-dev/pandas: Pandas*. Zenodo. https://doi.org/10.5281/zenodo.3509134

Pazzaglia, F. J. (2003). Landscape evolution models. In *Developments in Quaternary Sciences* (Vol. 1, pp. 247–274). Elsevier. https://doi.org/10.1016/S1571-0866(03)01012-1

Pelletier, J. D. (2013). 2.3 Fundamental principles and techniques of landscape evolution modeling. In J. F. Shroder (Ed.), *Treatise on geomorphology* (pp. 29–43). Academic Press. https://doi.org/10.1016/B978-0-12-374739-6.00025-7

Perron, J. T., Dietrich, W. E., & Kirchner, J. W. (2008). Controls on the spacing of first-order valleys. *Journal of Geophysical Research: Earth Surface*, *113*(4), 1–21. https://doi.org/10.1029/2007JF000977

Prancevic, J. P., & Kirchner, J. W. (2019). Topographic controls on the extension and retraction of flowing streams. *Geophysical Research Letters*, *46*(4), 1–21. https://doi.org/10.1029/2018GL081799

Riebe, C. S., Hahm, W. J., & Brantley, S. L. (2017). Controls on deep critical zone architecture: A historical review and four testable hypotheses. *Earth Surface Processes and Landforms*, *42*(1), 128–156. https://doi.org/10.1002/esp.4052

Roering, J. J. (2008). How well can hillslope evolution models "explain" topography? Simulating soil transport and production with high-resolution topographic data. *Geological Society of America Bulletin*, *120*(9–10), 1248–1262. https://doi.org/10.1130/B26283.1

Roering, J. J., Kirchner, J. W., & Dietrich, W. E. (1999). Evidence for nonlinear, diffusive sediment transport on hillslopes and implications for landscape morphology. *Water Resources Research*, *35*(3), 853–870. https://doi.org/10.1029/1998WR900090

Roering, J. J., Kirchner, J. W., & Dietrich, W. E. (2001). Hillslope evolution by nonlinear, slope-dependent transport: Steady state morphology and equilibrium adjustment timescales. *Journal of Geophysical Research: Solid Earth*, *106*(B8), 16499–16513. https://doi.org/10.1029/2001JB000323

Rosenbloom, N. A., & Anderson, R. S. (1994). Hillslope and channel evolution in a marine terraced landscape, Santa Cruz, California. *Journal of Geophysical Research: Solid Earth*, *99*(B7), 14013–14029. https://doi.org/10.1029/94JB00048

Sangireddy, H., Carothers, R. A., Stark, C. P., & Passalacqua, P. (2016). Controls of climate, topography, vegetation, and lithology on drainage density extracted from high resolution topography data. *Journal of Hydrology*, *537*, 271–282. https://doi.org/10.1016/j.jhydrol.2016.02.051

Snyder, N. P., Whipple, K. X., Tucker, G. E., & Merritts, D. J. (2003). Channel response to tectonic forcing: Field analysis of stream morphology and hydrology in the Mendocino triple junction region, northern California. *Geomorphology*, *53*(1), 97–127. https://doi.org/10.1016/S0169-555X(02)00349-5

Tarboton, D. G., Bras, R. L., & Rodriguez-Iturbe, I. (1989). Scaling and elevation in river networks. *Water Resources Research*, *25*(9), 2037–2051. https://doi.org/10.1029/WR025i009p02037

Temme, A. J. A. M., Schoorl, J. M., Claessens, L., & Veldkamp, A. (2013). 2.13 Quantitative modeling of landscape evolution. In J. F. Shroder (Ed.), *Treatise on geomorphology* (pp. 180–200). Academic Press. https://doi.org/10.1016/B978-0-12-374739-6.00039-7

Theodoratos, N., & Kirchner, J. W. (2020a). Dimensional analysis of a landscape evolution model with incision threshold. *Earth Surface Dynamics*, *8*(2), 505–526. https://doi.org/10.5194/esurf-8-505-2020

Theodoratos, N., & Kirchner, J. W. (2020b). Graphically interpreting how incision thresholds influence topographic and scaling properties of modeled landscapes. *Earth Surface Dynamics Discussions*, 1–25. https://doi.org/10.5194/esurf-2020-45

Theodoratos, N., Seybold, H., & Kirchner, J. W. (2018). Scaling and similarity of a stream-power incision and linear diffusion landscape evolution model. *Earth Surface Dynamics*, *6*(3), 779–808. https://doi.org/10.5194/esurf-6-779-2018

Tramblay, Y., Bouvier, C., Martin, C., Didon-Lescot, J.-F., Todorovik, D., & Domergue, J.-M. (2010). Assessment of initial soil moisture conditions for event-based rainfall–runoff modelling. *Journal of Hydrology*, *387*(3), 176–187. https://doi.org/10.1016/j.jhydrol.2010.04.006

Troch, P. A., Lahmers, T., Meira, A., Mukherjee, R., Pedersen, J. W., Roy, T., & Valdes-Pineda, R. (2015). Catchment coevolution: A useful framework for improving predictions of hydrological change? *Water Resources Research*, *51*(7), 4903–4922. https://doi.org/10.1002/2015WR017032

Troch, P. A., Paniconi, C., & Van Loon, E. E. (2003). Hillslope-storage Boussinesq model for subsurface flow and variable source areas along complex hillslopes: 1. Formulation and characteristic response. *Water Resources Research*, *39*(11). https://doi.org/10.1029/2002WR001728

Tsujimoto, T. (1999). Sediment transport processes and channel incision: Mixed size sediment transport, degradation and armoring. In S. E. Darby, & A. Simon (Eds.), *Incised river channels: Processes, forms, engineering, and management* (pp. 37–66). J. Wiley.

Tucker, G. E. (2004). Drainage basin sensitivity to tectonic and climatic forcing: Implications of a stochastic model for the role of entrainment and erosion thresholds. *Earth Surface Processes and Landforms*, *29*(2), 185–205. https://doi.org/10.1002/esp.1020

Tucker, G. E., & Bras, R. L. (1998). Hillslope processes, drainage density, and landscape morphology. *Water Resources Research*, *34*(10), 2751–2764. https://doi.org/10.1029/98WR01474

Tucker, G. E., Catani, F., Rinaldo, A., & Bras, R. L. (2001). Statistical analysis of drainage density from digital terrain data. *Geomorphology*, *36*(3), 187–202. https://doi.org/10.1016/S0169-555X(00)00056-8

Tucker, G. E., & Slingerland, R. (1997). Drainage basin responses to climate change. *Water Resources Research*, *33*(8), 2031–2047. https://doi.org/10.1029/97WR00409

Valters, D. (2016). Modelling geomorphic systems: Landscape evolution. In S. J. Cook, L. E. Clarke, & J. E. Nield (Eds.), *Geomorphological techniques* (p. 6.5.12). British Society for Geomorphology. https://doi.org/10.13140/RG.2.1.1970.9047

West, A. J., Galy, A., & Bickle, M. (2005). Tectonic and climatic controls on silicate weathering. *Earth and Planetary Science Letters*, *235*(1), 211–228. https://doi.org/10.1016/j.epsl.2005.03.020

Whipple, K. X. (2001). Fluvial landscape response time: How plausible is steady-state denudation? *American Journal of Science*, *301*(4–5), 313–325. https://doi.org/10.2475/ajs.301.4-5.313

Whipple, K. X., Hancock, G. S., & Anderson, R. S. (2000). River incision into bedrock: Mechanics and relative efficacy of plucking, abrasion, and cavitation. *Geological Society of America Bulletin*, *112*(3), 490–503.

Whipple, K. X., & Tucker, G. E. (1999). Dynamics of the stream-power river incision model: Implications for height limits of mountain ranges, landscape response timescales, and research needs. *Journal of Geophysical Research: Solid Earth*, *104*(B8), 17661–17674. https://doi.org/10.1029/1999JB900120

Willgoose, G., Bras, R. L., & Rodriguez-Iturbe, I. (1991a). A coupled channel network growth and hillslope evolution model: 1. Theory. *Water Resources Research*, *27*(7), 1671–1684. https://doi.org/10.1029/91WR00935

Willgoose, G., Bras, R. L., & Rodriguez-Iturbe, I. (1991b). A coupled channel network growth and hillslope evolution model: 2. Nondimensionalization and applications. *Water Resources Research*, *27*(7), 1685–1696. https://doi.org/10.1029/91WR00936

Willgoose, G., Bras, R. L., & Rodriguez-Iturbe, I. (1991c). A physical explanation of an observed link area-slope relationship. *Water Resources Research*, *27*(7), 1697–1702. https://doi.org/10.1029/91WR00937

Wohl, E., & David, G. C. L. (2008). Consistency of scaling relations among bedrock and alluvial channels. *Journal of Geophysical Research: Earth Surface*, *113*(F4). https://doi.org/10.1029/2008JF000989

Yoshida, T., & Troch, P. A. (2016). Coevolution of volcanic catchments in Japan. *Hydrology and Earth System Sciences*, *20*(3), 1133–1150. https://doi.org/10.5194/hess-20-1133-2016

Zhang, Y., Slingerland, R., & Duffy, C. (2016). Fully-coupled hydrologic processes for modeling landscape evolution. *Environmental Modelling and Software*, *82*, 89–107. https://doi.org/10.1016/j.envsoft.2016.04.014